communications biology

Article

https://doi.org/10.1038/s42003-024-07196-0

PLGA/BK microspheres targeting the bradykinin signaling pathway as a therapeutic strategy to delay intervertebral disc degeneration

Xiaoming Qiu[1,2,3,5], Yizhi Zhang[1,3,5], Ziyan Wei[1,3,5], Zhangbin Luo[1,3], Zhuanping Wang[1,4] & Xuewen Kang[1,3] ✉

Intervertebral disc degeneration(IVDD) is a common spinal condition with limited effective treatments available. This study aims to investigate the impact of poly(lactic-co-glycolic acid)/Bradykinin (PLGA/BK) microspheres on IVDD and its underlying mechanisms. We collected nucleus pulposus samples from both healthy and degenerated human intervertebral disks and conducted immunohistochemical analyses, revealing reduced BK expression in degenerated tissues. Subsequently, we used BK to treat nucleus pulposus cells and conducted Bulk RNA sequencing (RNA-seq), identifying BK's involvement in cellular senescence, extracellular matrix metabolism, and the PI3K signaling pathway. Further experiments using tert-butyl hydroperoxide (TBHP)-induced cell senescence showed that BK treatment reduced senescence, enhanced extracellular matrix synthesis, and inhibited degradation, along with activation of the PI3K pathway. These effects were mediated through B2R (BK receptor 2) and the downstream PI3K pathway. Following this, we developed sustained-release BK microspheres with an optimized manufacturing process. In vitro co-culture experiments showed no observable toxicity. We established an IVDD model in rat tail vertebrae through fine needle puncture, administering local injections of BK sustained-release microspheres. Using various experimental methods, including X-ray, MRI, histopathology, and immunohistochemistry, we found that these microspheres could slow the progression of IVDD. This study highlights the potential of injectable PLGA/BK microspheres to regulate cellular senescence and extracellular matrix metabolism via the B2R and PI3K pathways, ultimately delaying IVDD.

Intervertebral disc degeneration (IVDD) represents a prevalent spinal ailment, with multifaceted etiological factors encompassing age-related changes, biomechanical stresses incurred during posture maintenance and ambulation, and genetic regulatory mechanisms[1–4]. Nonetheless, the precise causative factors and the intricate regulatory pathways governing IVDD remain elusive. Some literature has noted that the human spine undergoes progressive degeneration from as early as the third decade of life[5]. In youth, the intervertebral disc's nucleus pulposus retains adequate hydration and thickness. However, as individuals age, the intervertebral disc progressively becomes brittle, losing elasticity and moisture. This process leads to disc thinning and degeneration, subsequently affecting the adjacent vertebrae's structure and functionality[6,7]. Consequentially, IVDD can culminate in intervertebral arthritis, bone hyperplasia, spinal stenosis, and related maladies, manifesting as symptoms such as low back pain, neck pain, and sciatica, thus significantly impairing the quality of life and work capacity for individuals globally[8]. In clinical practice, physicians frequently resort to non-steroidal anti-inflammatory drugs like ibuprofen, indomethacin, and diclofenac to alleviate the inflammatory and painful manifestations of IVDD[9,10].

[1]Lanzhou University Second Hospital, Lanzhou, Gansu, PR China. [2]Gansu Provincial Hospital of TCM (The First Affiliated Hospital of Gansu University of Chinese Medicine), Gansu University of Chinese Medicine, Lanzhou, Gansu, PR China. [3]Orthopaedics Key Laboratory of Gansu Province, Lanzhou, Gansu, PR China. [4]Department of Endocrinology, Lanzhou University Second Hospital, Lanzhou, Gansu, PR China. [5]These authors contributed equally: Xiaoming Qiu, Yizhi Zhang, Ziyan Wei. ✉e-mail: ery_kangxw@lzu.edu.cn

Regrettably, these medications are systemic and oral in nature, lacking specificity for IVDD treatment or progression delay[11]. When conservative measures fail or symptoms worsen, surgical intervention may be necessary, bearing its own set of associated risks and complications[12,13]. Thus, there exists a pressing need for the development of targeted and efficacious therapeutics precisely tailored to IVDD.

A recent study has spotlighted kininogen 1 as a pivotal gene within aging nucleus pulposus cells (NPCs)[14]. KNG-1 constitutes a crucial component of the kallikrein-kinin system (KKS), which encompasses kallikrein, kinins, and their corresponding receptors, exerting pivotal roles in numerous physiological and pathological processes, including inflammation, vasodilation, and cellular proliferation[15–17]. A review of extant literature underscores its plausible links to factors contributing to IVDD, thereby piquing our interest in investigating the KKS's involvement in IVDD. Among kinins, bradykinin(BK) stands out as the principal player within the KKS, serving essential physiological functions. Our previous research findings have indicated that BK promotes cellular proliferation, mitigates oxidative stress, and curtails apoptosis. It is noteworthy that BK has been associated with the aging process[18], although a definitive link between BK and intervertebral disks or NPCs, and their potential role in IVDD, remains incompletely understood.

The primary objective of this study is to elucidate BK's potential role in IVDD and the underlying mechanisms, with an ultimate goal of harnessing BK as a peptide in IVDD treatment. To this end, our research commences with a comprehensive investigation encompassing human clinical samples and animal experimental models to ascertain the presence of BK in intervertebral disc tissue and its potential correlation with IVDD initiation and progression. In the following steps, we employ targeted BK stimulation of NPCs to evaluate its impact on cellular senescence, extracellular matrix synthesis, and degradation. Furthermore, to facilitate precise local drug delivery, we explore the formulation of PLGA/BK sustained-release microspheres and optimize their production processes, envisioning novel avenues for future IVDD treatment strategies.

We firmly believe that by exploring BK's role in IVDD, we can enhance our comprehension of the ailment's pathogenesis, ultimately affording a robust scientific foundation for the development of innovative therapeutic strategies. This, in turn, holds the potential to ameliorate patients' quality of life and alleviate the global healthcare burden imposed by IVDD.

Results

Downregulation of BK expression in degenerated intervertebral disks

In this study, we procured ten clinical human intervertebral disc specimens, comprising five cases of severe degeneration and five cases of mild degeneration (Fig. 1B). These specimens of the human nucleus pulposus were subjected to HE staining, and microstructural observations were conducted at 200× and 400× magnifications, respectively (Fig. 1A).

In mild-degenerated nucleus pulposus tissue, a normative arrangement of collagen fibers, lightly stained cell cytoplasm, and extracellular matrix were observed, with no notable cell aggregation. Conversely, in severely degenerated nucleus pulposus tissue, aging-associated alterations led to deep eosin staining, accompanied by multiple cell agglomerations. Notably, the pathological HE staining and Pfirrmann grading consistently reflected the degree of degeneration.

IHC was employed to identify BK and Kallikrein, a pivotal enzyme promoting BK release. These markers were detected in both human nucleus pulposus tissue types but exhibited diminished expression in severely degenerated nucleus pulposus tissue (Fig. 1A, C and D). WB was subsequently employed to assess the expression of extracellular matrix anabolic Aggrecan, catabolic MMP-3/MMP-9, and senescence marker P53, corroborating the degeneration status at the molecular level. These findings aligned with the Pfirrmann grading results (Fig. 1E and F).

Bulk RNA-seq in BK-intervened NPCs

Principal Component Analysis (PCA) of gene expression profiles from bulk RNA-seq of BK-treated rat NPCs and the control group indicated significant dissimilarities between the two datasets (Fig. 2A). Subsequent differential gene analysis identified 22 genes with marked differences (adjusted $P < 0.05$ using the False Discovery Rate (FDR) method) in BK-intervened NPCs (Figs. 2B and C). Among these genes, 12 were notably upregulated in the BK intervention group compared to the control group (Fig. 2D), while 10 exhibited reduced expression in the BK intervention group (Fig. 2E).

Functional enrichment analysis revealed that the biological processes (BP) influenced by these differentially expressed genes primarily encompassed cell migration, cell differentiation, neuron axon guidance, angiogenesis, bone formation, and immune cell chemotaxis. These processes are integral to organismal development, repair, and normal functioning (Fig. 2F). In terms of cellular components (CC), the differentially expressed genes were primarily associated with cell membranes, protein complexes, neuronal structures, muscle structures, and extracellular matrix components. These cellular structures and complexes play pivotal roles in cellular functions, signal transduction, neurotransmitter release, tissue architecture, and other biological processes (Fig. 2G). Regarding molecular functions (MF), the enriched categories encompass enzyme activity, protein binding, cell signaling, and receptor activity. These molecular activities are central to biological processes such as cell signaling, growth factor regulation, cell adhesion, and lipid metabolism (Fig. 2H).

Moreover, KEGG pathway analysis unveiled that the differentially expressed genes were predominantly enriched in pathways related to extracellular matrix-receptor interactions, affecting cell adhesion and signaling, growth hormone-mediated growth and development, nitrogen metabolism, and osteoclast differentiation. These pathways are critical for bone health and the regulation of cellular functions, including the PI3K-Akt and TNF signaling pathways (Fig. 2I).

BK regulation of cell senescence, extracellular matrix metabolism, and the PI3K/AKT pathway

The application of β-galactosidase staining can be used as an indicator to reflect the senescence state of cells. Upon induction of senescence in NPCs with TBHP, an increase in β-galactosidase staining was observed (Fig. 3A). However, pretreatment with BK led to a notable reduction in the number of blue-stained cells. Quantitative analysis further confirmed that BK effectively attenuated TBHP-induced cellular senescence (Fig. 3B). Molecular markers of senescence, including P16, P21, and P-P53, substantiated the inhibitory effect of BK on TBHP-induced senescence (Fig. 3C–F).

Alterations in cell functionality within the nucleus pulposus can result in changes in extracellular matrix protein composition. Enhanced catabolism and diminished anabolism are pivotal factors contributing to reduced protein content and water content in the intervertebral disc's nucleus pulposus, thereby accelerating degeneration. The equilibrium between anabolic and catabolic proteins jointly regulates the protein components within the extracellular matrix, with Aggrecan and Collagen-II being principal anabolic proteins.

Immunofluorescence technology was employed to fluorescently label and stain Aggrecan within cells (Fig. 3G). Brightness analysis indicated that the BK-treated group exhibited increased fluorescence brightness, while TBHP-induced cells displayed decreased fluorescence intensity. BK pretreatment mitigated the reduction in fluorescence intensity induced by TBHP. Statistical quantification of average fluorescence intensity confirmed BK's capacity to promote Aggrecan synthesis (Fig. 3H). Molecular insights were provided through WB, which reasserted that BK enhanced extracellular matrix anabolic markers, including Aggrecan and Collagen-II (Fig. 3I–K).

In contrast, catabolic processes are characterized by proteins like MMP-3 and MMP-9. MMP-9, a principal catabolic protein, was fluorescently labeled and stained using immunofluorescence technology (Fig. 3L).

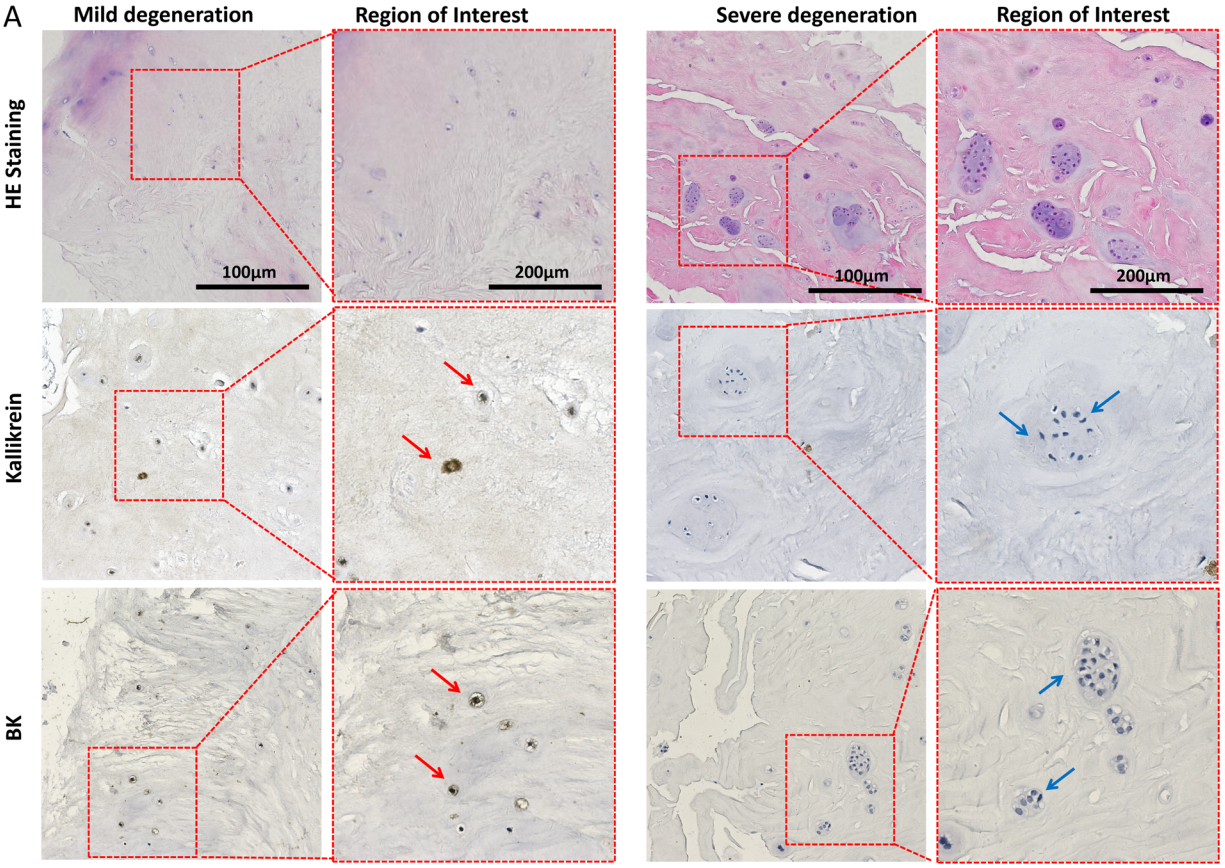

B

Sex	Age (years)	Degenerative grades
Female	12	I
Male	15	I
Female	27	II
Female	28	II
Male	38	II
Male	71	III
Female	51	IV
Female	67	IV
Female	50	V
Male	71	V

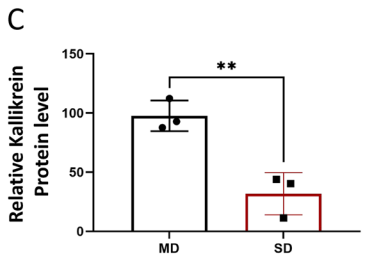

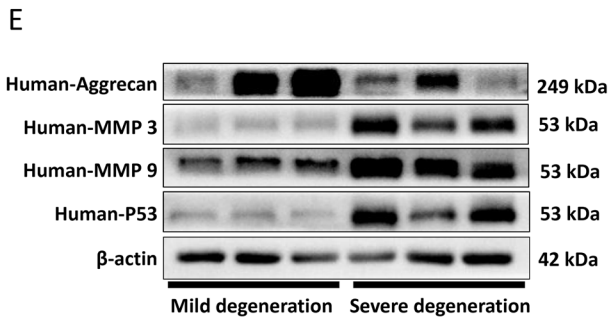

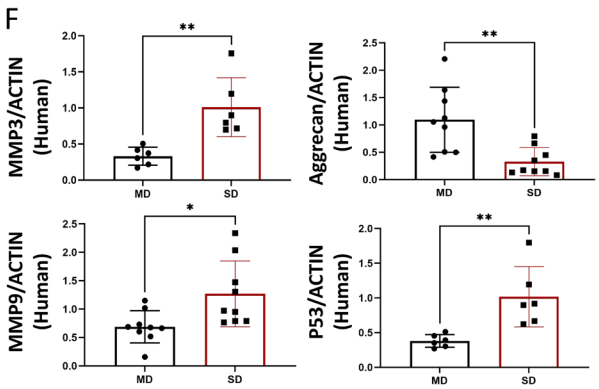

Fig. 1 | Histological and protein expression analysis of nucleus pulposus tissue in mildly and severely degenerated samples. A HE staining of mildly and severely degenerated nucleus pulposus tissue sections, with immunohistochemical staining for Kallikrein and BK. Red arrows indicate positive cells and blue arrows indicate negative cells. **B** Basic information of collected human nucleus pulposus specimens. **C**, **D** Relative expression of BK and Kallikrein proteins in mildly and severely degenerated tissues. **E** Western blot detection of Aggrecan, MMP-3, MMP-9, and P53 proteins in mildly and severely degenerated nucleus pulposus tissue. **F** Quantitative analysis of protein expression. Mild degeneration (MD), severe degeneration (SD). To assess the statistical differences between various groups, we employed one-way analysis of variance (ANOVA) followed by Tukey's post hoc test for multiple comparisons (*$p < 0.05$, **$p < 0.01$, ***$p < 0.001$, ****$p < 0.0001$). Mechanism diagram: PLGA/BK Microspheres Targeting the Bradykinin Signaling Pathway as a Therapeutic Strategy to Delay Intervertebral Disc Degeneration.

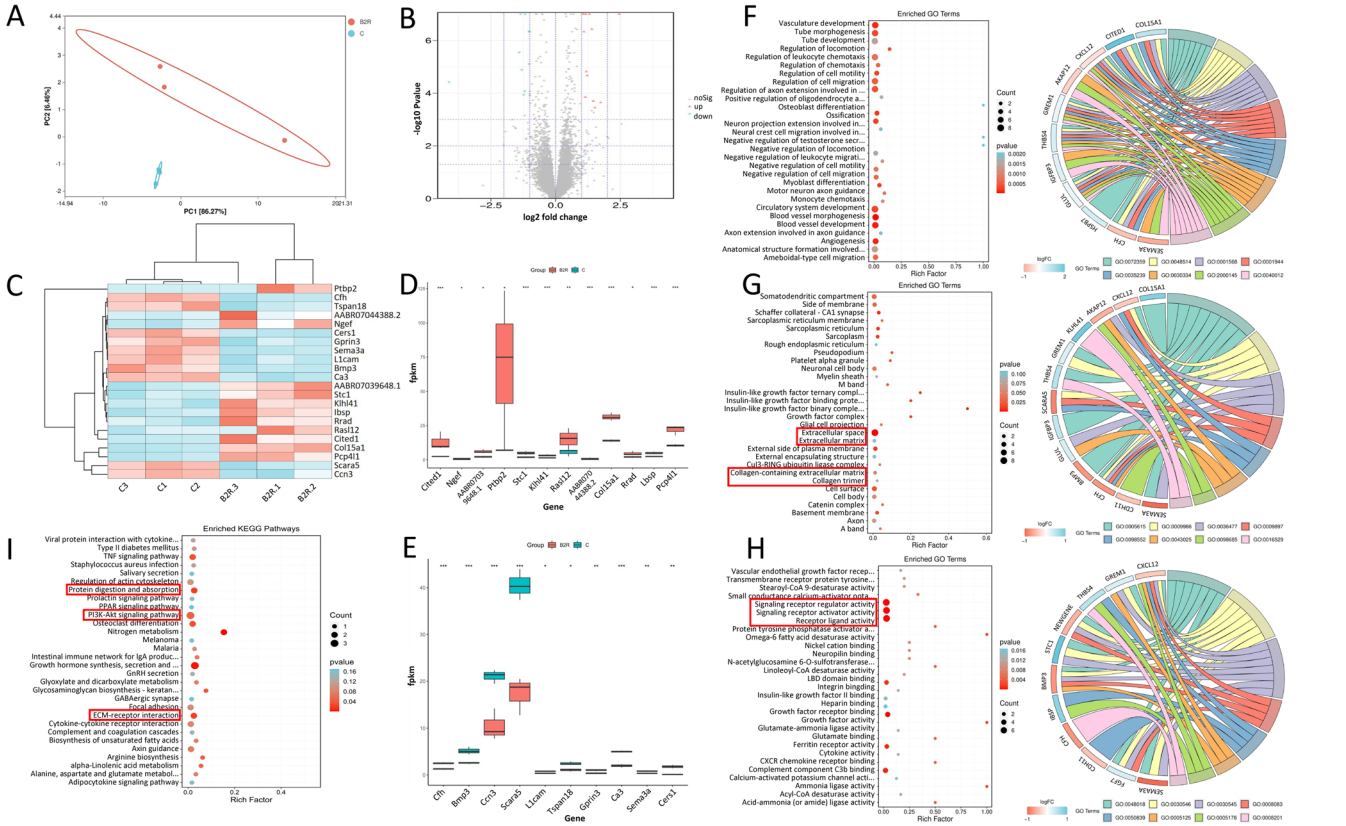

Fig. 2 | Gene expression profiling and functional annotation of BK intervention in nucleus pulposus cells. **A** Principal Component Analysis (PCA) of gene expression profiles. **B** Volcano plot illustrating the differential gene screening with adjusted P-values. **C** Cluster analysis of genes with significant upregulation and downregulation in the BK intervention group. **D** Histogram showing the top 12 upregulated genes in the BK intervention group. **E** Histogram showing the top 10 downregulated genes in the BK intervention group. **F** Biological Process (BP) analysis bubble diagram and chord diagram for differentially expressed genes. **G** Cellular Component (CC) analysis bubble diagram and chord diagram for differentially expressed genes. **H** Molecular Function (MF) analysis bubbles and chord diagram for differentially expressed genes. **I** KEGG pathway enrichment analysis of differentially expressed genes (*: adjusted $P < 0.05$, **: adjusted $P < 0.01$, ***: adjusted $P < 0.001$, ****: adjusted $P < 0.0001$).

The BK-treated group exhibited reduced fluorescence brightness, while TBHP-induced cells showed an increase in fluorescence intensity. BK pretreatment alleviated the heightened fluorescence intensity induced by TBHP. Quantitative analysis confirmed that TBHP upregulated MMP-9 expression and exacerbated catabolism (Fig. 3M). WB analysis further validated BK's ability to inhibit the elevation of extracellular matrix catabolic markers, including MMP-3 and MMP-9 (Fig. 3N–P).

Furthermore, WB analysis substantiated that PI3K/AKT phosphorylation in NPCs exposed to TBHP decreased, whereas BK treatment enhanced PI3K/AKT phosphorylation, thereby activating the PI3K/AKT signaling pathway(Fig. 3Q–U). It is consistent with the conclusion of previous KEGG pathway enrichment analysis.

Assessing the beneficial cellular effects of BK after B2R and PI3K inhibition

To ascertain the involvement of the B2R and the PI3K/AKT signaling pathways in mediating the cellular effects of BK and to delve deeper into its mechanistic actions, we employed blockers targeting B2R and PI3K/AKT signaling in NPCs. We conducted senescence-associated SA-β-gal staining to assess cellular senescence (Fig. 4A and B) and examined the relative protein expression of aging molecular markers, including P-P53, P21, and P16 (Fig. 4C–F). Our findings conclusively demonstrated that the salutary effects of BK in mitigating NPC aging were abolished upon B2R blockade. In addition, the anti-aging properties of BK were found to be compromised when the PI3K/AKT pathway was inhibited with LY294002.

Additionally, upon blocking B2R and the PI3K/AKT pathways in NPCs, we assessed Aggrecan immunofluorescence intensity and evaluated the relative protein expression of anabolic molecular markers, specifically Aggrecan and Collagen-II (Fig. 4G, K). Notably, the advantageous impact of BK in promoting extracellular matrix anabolism among NPCs was nullified following B2R blockade. Similarly, when the PI3K/AKT pathway was obstructed with LY294002, BK was unable to exert its beneficial effects in enhancing extracellular matrix synthesis.

Likewise, subsequent to the inhibition of B2R and the PI3K/AKT signaling pathways in NPCs, we quantified MMP-9 immunofluorescence intensity and assessed the relative protein expression of catabolic molecular markers, specifically MMP-3 and MMP-9 (Fig. 4L–P). Our results unambiguously established that BK's favorable effects on reducing extracellular matrix catabolism among NPCs were compromised under these conditions. Additionally, we observed that antagonizing B2R resulted in the inability of BK to activate the PI3K/AKT pathway. Similarly, when the PI3K/AKT pathway was blocked using LY294002, BK also failed to exert its beneficial protective effects (Fig. 4Q–U).

Preparation and characterization of PLGA/BK microspheres

Previous results have conclusively demonstrated that bradykinin (BK) plays a crucial role in the progression of intervertebral disc degeneration. The introduction of exogenous BK may have a positive impact on this process. Based on these findings, we have prepared PLGA microspheres containing BK, and plan to conduct a series of comprehensive evaluations on their morphology, structure, drug release profiles, and therapeutic effects in upcoming experiments. These studies aim to validate the potential efficacy and safety of PLGA/BK microspheres as a treatment for intervertebral disc degeneration.

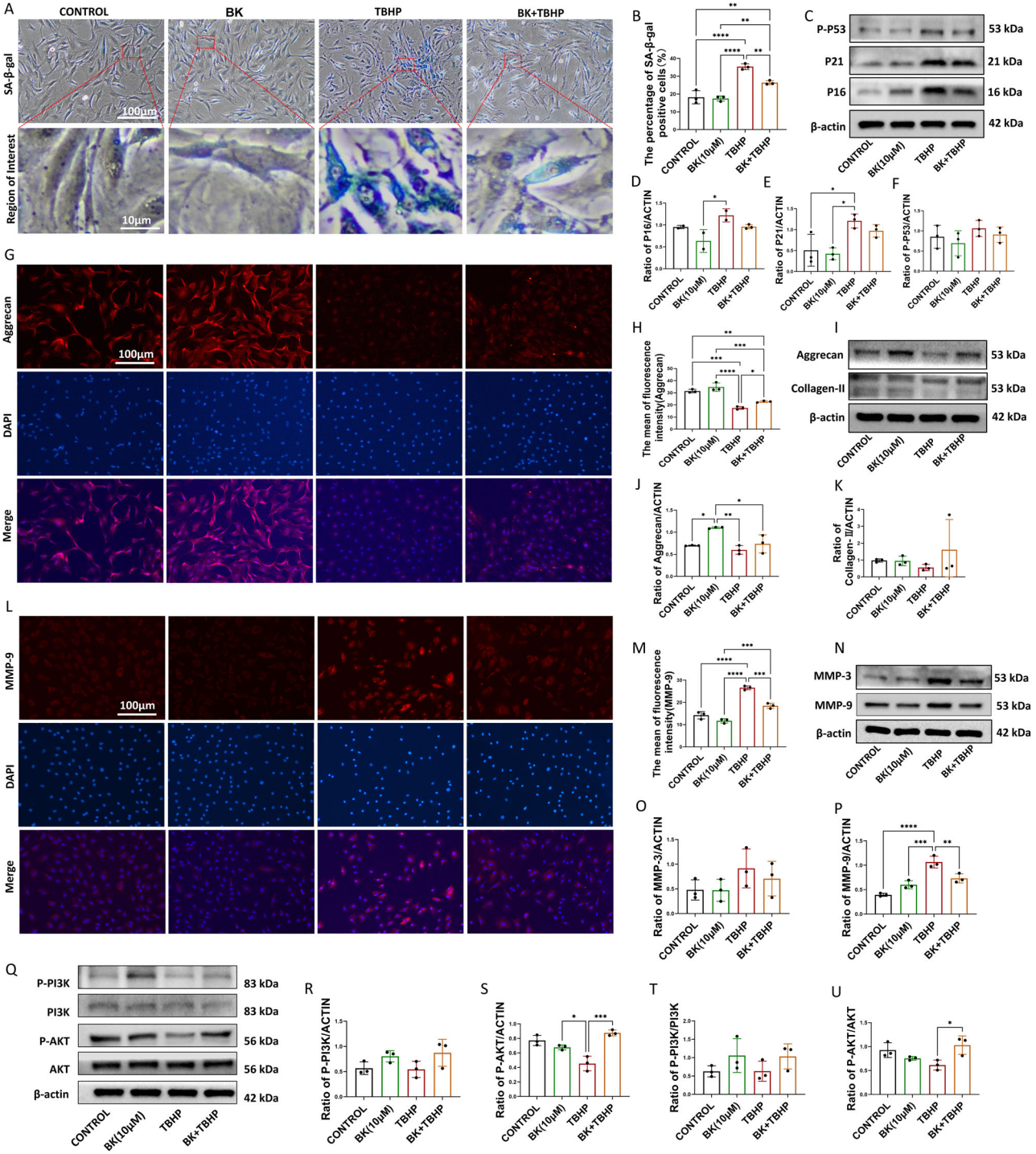

Fig. 3 | Effects of BK treatment on cell senescence and extracellular matrix protein expression in nucleus pulposus cells. A Expression of cell senescence staining after TBHP and BK treatment at 100x and 1000x magnification. **B** Quantitative statistics of positive cells after senescence staining. **C** Western blot analysis of P16, P21 and P-P53 in cells treated with BK and TBHP. **D**–**F** Quantitative analysis of P16, P21 and P-P53 expression levels. **G** Aggrecan immunofluorescence staining of cells after TBHP and BK treatment at 200x magnification. **H** Quantitative statistics of the average immunofluorescence intensity of cells in each experimental group. **I** Western blot analysis of Aggrecan and Collagen-II in cells treated with BK and TBHP. **J**, **K** Quantitative analysis of Aggrecan and Collagen-II expression levels. **L** MMP9 immunofluorescence staining of cells after TBHP and BK treatment at 200x magnification. **M** Quantitative statistics of the average immunofluorescence intensity of cells in each experimental group. **N** Western blot analysis of MMP-3 and MMP-9 in cells treated with BK and TBHP. **O**, **P** Quantitative analysis of Aggrecan and Collagen-II expression levels. **Q** Western blot analysis of PI3K, P-PI3K, AKT and P-AKT in cells treated with BK and TBHP. **R**–**U** Quantitative analysis of P-PI3K/ACTIN, P-AKT/ACTIN, P-PI3K/PI3K, and P-AKT/AKT ratios. To assess the statistical differences between various groups, we employed one-way analysis of variance (ANOVA) followed by Tukey's post hoc test for multiple comparisons (*: $p < 0.05$, **: $p < 0.01$, ***: $p < 0.001$, ****: $p < 0.0001$). There are no significant statistical differences in Fig. 3F, K, O, and R.

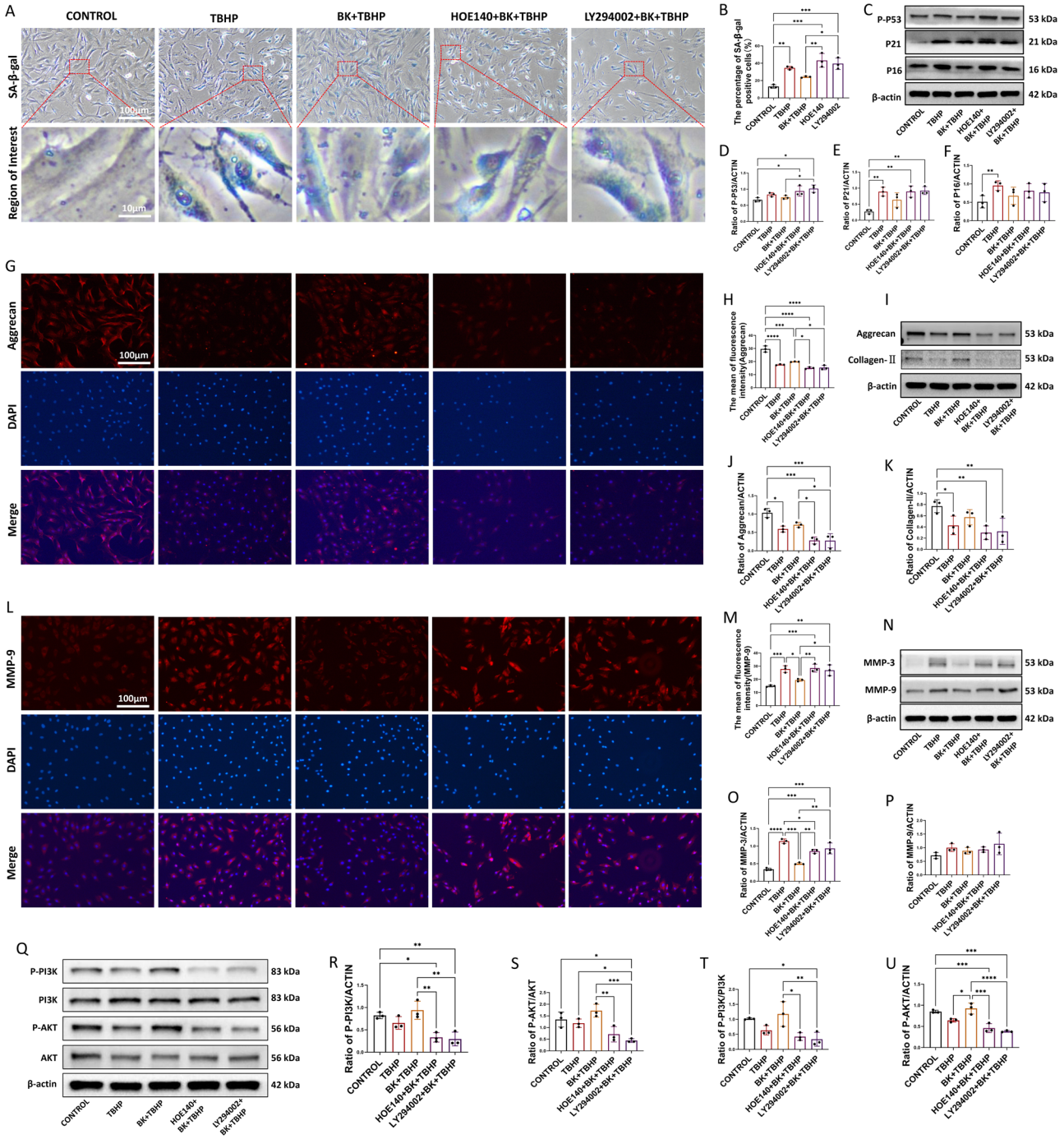

Fig. 4 | Inhibition of BK-mediated anti-aging and metabolic effects in nucleus pulposus cells by HOE140 and LY294002. A, **B** SA-β-gal senescence staining and quantitative analysis of senescent cell counts. HOE140 and LY294002 can block the anti-aging effect of BK. **C**–**F** Western blot analysis and quantitative statistical analysis of the expression of senescence markers P-P53, P21 and P16 in NPCs. **G**, **H** Aggrecan immunofluorescence and quantitative analysis of fluorescence intensity of cells. HOE140 and LY294002 can block the anabolic-promoting effect of BK. **I**–**K** Western blot analysis and quantitative statistical analysis of the expression of extracellular matrix anabolic markers Aggrecan and Collagen-II in NPCs. **L**, **M** MMP-9 immunofluorescence and quantitative analysis of fluorescence intensity of cells. HOE140 and LY294002 can block the effect of BK on reducing extracellular matrix catabolism of NPCs. **N**–**P** Western blot analysis and quantitative statistical analysis of the expression of extracellular matrix catabolism markers MMP-3 and MMP-9 in NPCs. **Q** Western blot analysis of the expression of PI3K, p-PI3K, AKT and pAKT in NPCs. **R**–**U** Quantitative analysis of P-PI3K/ACTIN, P-AKT/AKT, P-PI3K/PI3K and P-AKT/ACTIN levels.

Microsphere observation preceding experimental studies

Following an overnight stirring process to facilitate methylene chloride evaporation, the resultant microspheres within the beaker exhibited a visually consistent appearance as fine, white powder suspended in the polyvinyl alcohol (PVA) solution. Notably, these microspheres had the tendency to settle at the bottom of the beaker if left undisturbed. To further characterize their properties, a minute quantity of the microsphere suspension was drawn using a pipette and deposited onto a glass slide. Subsequent microscopic examination revealed that these microspheres exhibited a spherical morphology, with an approximate particle size of 100 μm Following an overnight stirring process to facilitate methylene chloride evaporation, the resultant microspheres within the beaker exhibited a visually consistent appearance as fine, white powder suspended in the polyvinyl alcohol (PVA) solution. Notably, these microspheres had the tendency to settle at the bottom of the

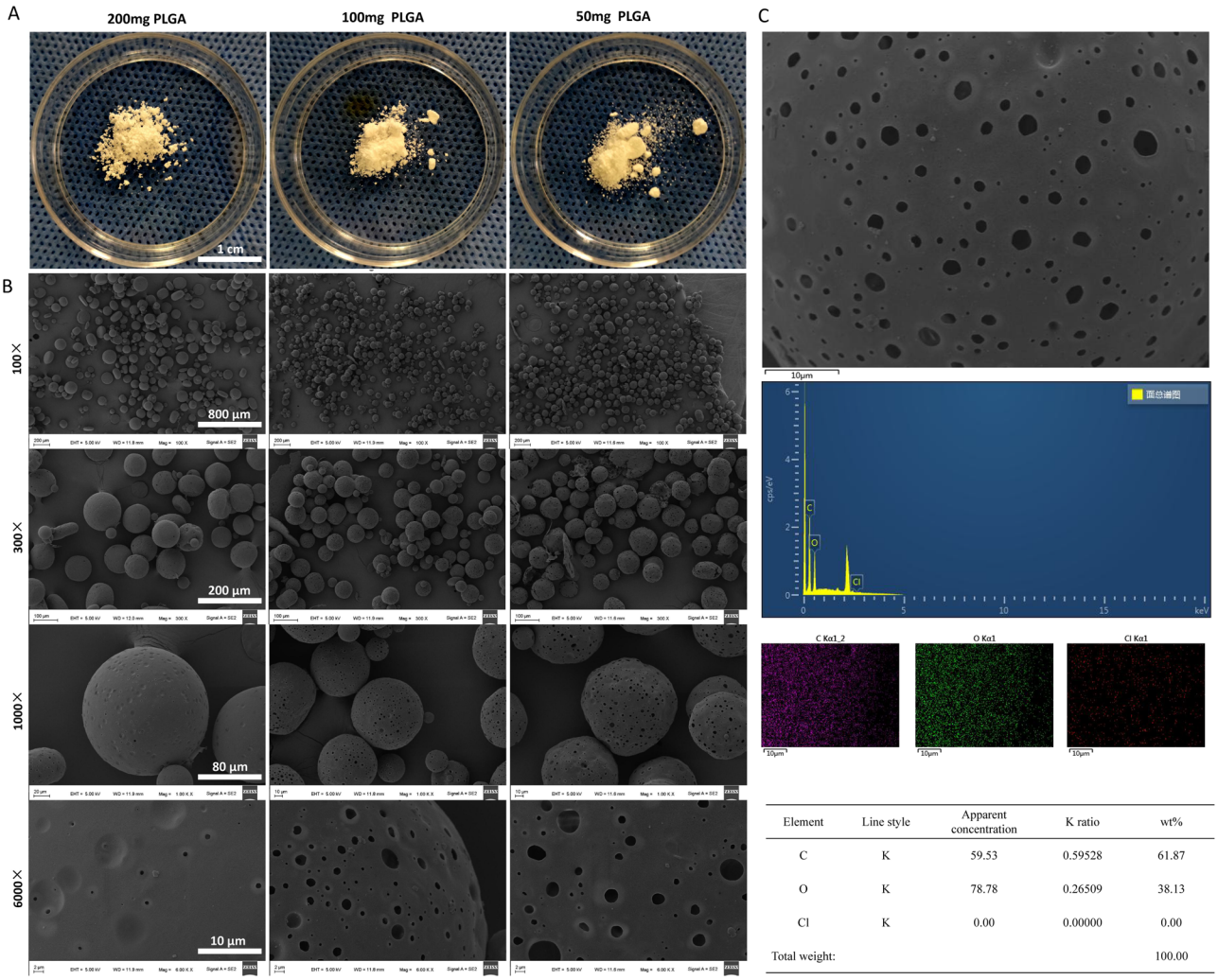

Element	Line style	Apparent concentration	K ratio	wt%
C	K	59.53	0.59528	61.87
O	K	78.78	0.26509	38.13
Cl	K	0.00	0.00000	0.00
Total weight:				100.00

Fig. 5 | Morphological characterization and surface element analysis of PLGA microspheres. A After optimization, with all other conditions held constant, naked-eye images of microspheres were taken when using 200 mg, 100 mg, and 50 mg of PLGA as input material. **B** Electron microscope images were captured at magnifications of 100×, 300×, 1000×, and 6000×. **C** Surface element analysis was conducted on microspheres prepared using 100 mg of PLGA, as scanned under an electron microscope.

beaker if left undisturbed. To further characterize their properties, a minute quantity of the microsphere suspension was drawn using a pipette and deposited onto a glass slide. Subsequent microscopic examination revealed that these microspheres exhibited a spherical morphology, with an approximate particle size of 100 μm (Fig. S2). It is imperative to underscore that the encapsulation rate and drug loading rate serve as pivotal metrics for assessing the quality of microspheres. Hence, to optimize the microsphere preparation methodology and select the optimal formulation for subsequent experiments, orthogonal optimization was undertaken.

. It is imperative to underscore that the encapsulation rate and drug loading rate serve as pivotal metrics for assessing the quality of microspheres. Hence, to optimize the microsphere preparation methodology and select the optimal formulation for subsequent experiments, orthogonal optimization was undertaken.

Establishment of a standard curve

Employing HPLC analysis at a wavelength of 214 nm (Fig. S3), we constructed a standard curve for BK based on calculated data (Fig. S4). The resulting regression equation was determined as follows: $y = 8E\text{-}05x\text{-}1.216$, yielding an R^2 value of 0.9998. This equation establishes a robust linear relationship between BK concentration within the range of 0.625 μg/ml to 640 μg/ml. Consequently, this equation was utilized to calculate and determine the drug loading rate and drug release rate of BK microspheres.

Orthogonal optimization design of microsphere preparation

Microspheres were systematically evaluated based on their encapsulation rate (Table S1) and drug loading rate (Table S2). A comprehensive assessment, as presented in Table S4, elucidates that the primary factor significantly influencing encapsulation rate is the quantity of PLGA added, with an optimal addition amount of 100 mg. Additionally, the optimal concentration of PVA in the external aqueous phase was determined to be 1.5%, and the stirring speed was maintained at 400 revolutions per minute (rpm). In contrast, the amount of drug added exerted relatively minor influence on encapsulation efficiency.

Furthermore, drug loading rate represents a critical indicator of microsphere efficacy. Upon calculating the drug loading rate for each experimental group, orthogonal experimental analysis outcomes (Table S5) underscore that the quantity of added drug exerts the most substantial impact on the drug loading rate. Following this, the PVA concentration and PLGA input amount emerge as the subsequent influential factors, while the stirring speed demonstrated the least effect on the drug loading rate of the microspheres.

Considering the aforementioned findings, the optimal conditions for microsphere preparation were determined as A2, B2, C3, and D1, signifying an input quantity of 100 mg for PLGA, 0.5 mg for BK, 1.5% for PVA concentration, and a stirring rate of 400 rpm.

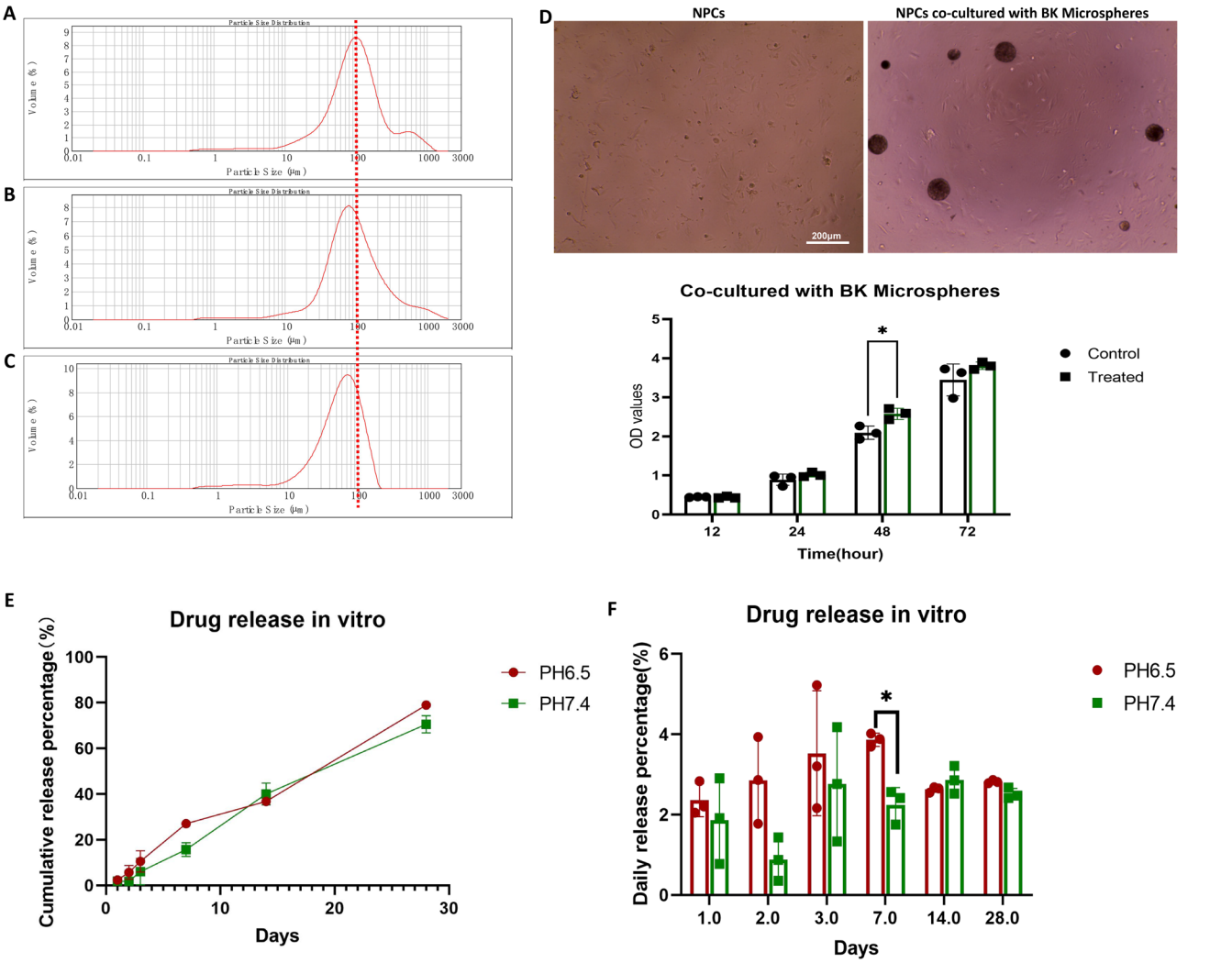

Fig. 6 | Characterization, cell co-culture, and drug release of PLGA/BK microspheres. A Particle size distribution of microspheres with an input of 200 mg of PLGA, with a median particle size of 95 μm. **B** Particle size distribution of microspheres with an input of 100 mg of PLGA, with a median particle size of 87 μm. **C** Particle size distribution of microspheres with an input of 50 mg of PLGA, with a median particle size of 60 μm. **D** Images of isolated cell groups, co-culture of microspheres and cells in a 96-well plate, and CCK-8 results for PLGA/BK microspheres co-cultured with primary rat NPCs for 3 days in vitro. **E**, **F** In vitro drug release of PLGA/BK microspheres in PBS with different pH. **E** Cumulative drug release from the microspheres. **F** Average daily drug release from the microspheres.

Characterization, encapsulation efficiency, drug loading rate, and drug release of optimized microspheres

Considering that the concentration of PLGA significantly influences encapsulation efficiency, a single-factor investigation was conducted by employing three different PLGA input concentrations while maintaining the optimal conditions. Characterization, encapsulation efficiency, drug loading rate, and drug release of the produced microspheres were systematically assessed using electron microscopy, laser particle size analysis, and HPLC (Fig. 5).

The morphology of microspheres

After optimization, with all other conditions held constant, the microspheres produced under varying PLGA input quantities (200 mg, 100 mg, and 50 mg) were visually inspected in a petri dish. These microspheres exhibited a uniform white powder appearance with consistent texture and well-dispersed distribution. Notably, as the input amount of PLGA decreased, the particle size of the microspheres also diminished (Fig. 5A).

A sample of PLGA/BK microspheres that had undergone centrifugation, washing, and freeze-drying under the optimized conditions was chosen for observation under a scanning electron microscope (Fig. 5B). The microspheres predominantly assumed regular spherical shapes, and as the input amount of PLGA decreased, their particle size decreased while larger surface pores became evident. Surface elemental analysis of the microspheres revealed a chlorine content of 0% under all three conditions (Fig. 5C).

Particle size distribution of microspheres

Utilizing a laser particle size analyzer, the microspheres produced with varying PLGA concentrations (200 mg, 100 mg, and 50 mg) were scanned and analyzed. Notably, the particle size of PLGA/BK microspheres exhibited a diminishing trend as the PLGA content decreased (Fig. 6A–C).

Microsphere encapsulation rate, drug loading rate, and drug release

Microspheres generated using PLGA input amounts of 200 mg, 100 mg, and 50 mg were dissolved and subjected to extraction with dichloromethane. Subsequently, HPLC was employed to determine the drug content within the microspheres, and the results were analyzed (Table S6). It is evident that the input amount significantly influences the particle size of microspheres. An optimal PLGA input quantity significantly enhances BK encapsulation efficiency within the microspheres. Specifically, under the conditions of 100 mg PLGA input, 0.5 mg BK input, 1.5% PVA concentration, and a stirring speed of 400 rpm, microspheres with an encapsulation rate of

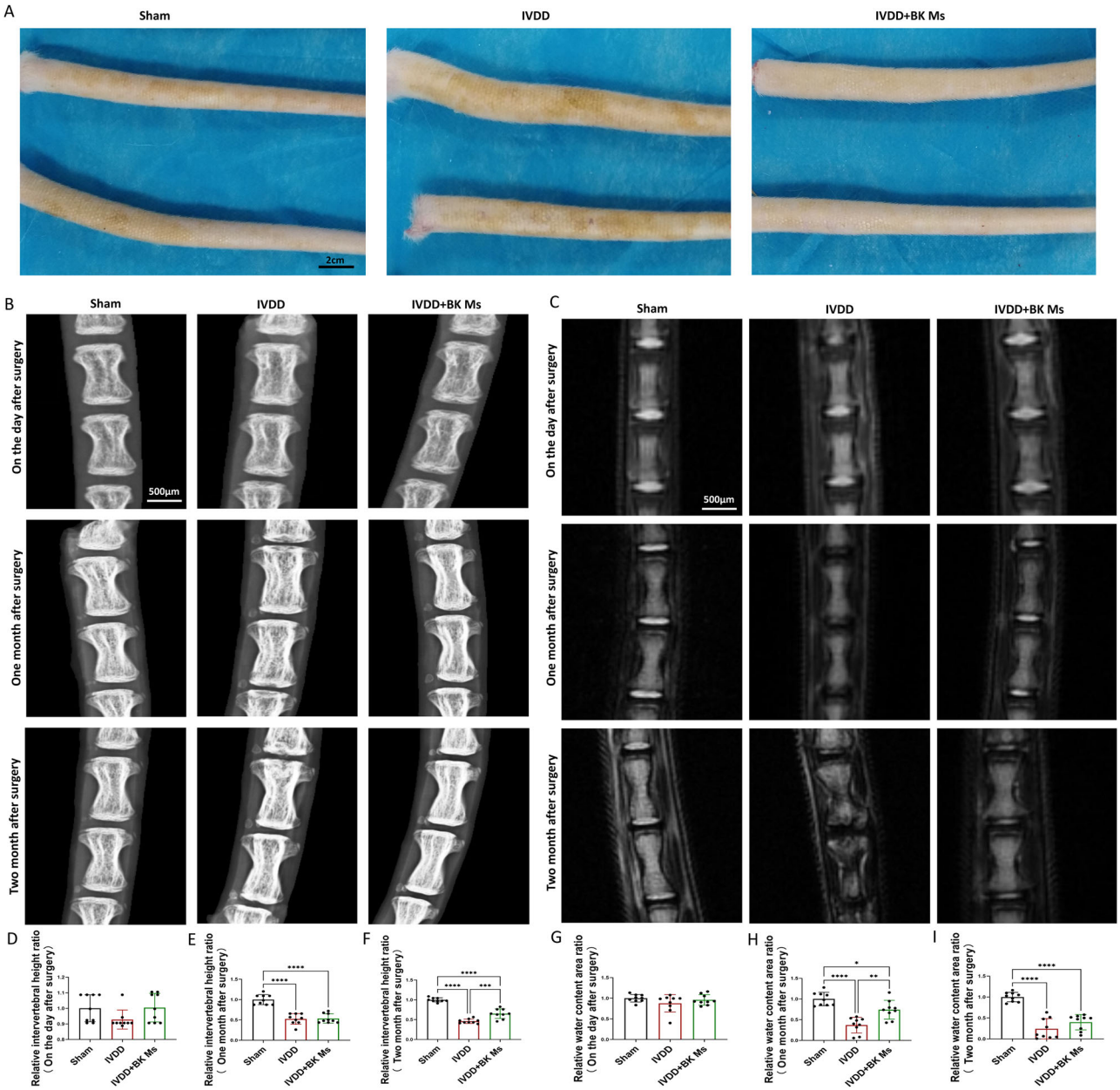

Fig. 7 | Post-surgical assessment of tail conditions in mice: X-ray, MRI, and intervertebral disc analysis. A General photos of the tails of mice in each experimental group 2 months after surgery. **B** X-ray performance of tails of mice in each experimental group after surgery, 1 month, and 2 months. **C** MR performance of tails of mice in each experimental group on the day after surgery, 1 month, and 2 months. **D** Intervertebral disc height ratio one day after surgery. **E** Intervertebral disc height ratio one month after surgery. **F** Intervertebral disc height ratio two months after surgery. **G** Relative moisture content one day after surgery. **H** Relative moisture content one month after surgery. **I** Relative moisture content two months after surgery. To assess the statistical differences between various groups, we employed one-way analysis of variance (ANOVA) followed by Tukey's post hoc test for multiple comparisons (*: $p < 0.05$, **: $p < 0.01$, ***: $p < 0.001$, ****: $p < 0.0001$). At each time point, each group consisted of three rats (n = 3).

74.10 ± 9.17% were produced. The microspheres prepared under these optimal conditions were subjected to in vitro drug release experiments in phosphate-buffered saline (PBS) with differing pH values (6.5 and 7.4) (Fig. 6E and F).

In vitro biocompatibility of PLGA/BK microspheres

In vitro co-culturing of PLGA/BK microspheres with primary rat NPCs over a 3-day period was performed (Fig. 6D). Results from the CCK-8 assay indicated that, compared to the control group, the PLGA/BK microsphere group demonstrated a slight enhancement in cell proliferation at various time points, and with no discernible reduction in cell viability. These findings highlight the absence of significant toxicity in vitro associated with PLGA/BK microspheres, thereby rendering them suitable for subsequent in vivo experimentation.

Effects of PLGA/BK microspheres on IVDD

General observations. Throughout the experiment, the experimental rats exhibited normal eating and resting habits in their recovery cages after surgery, displaying no restrictions in their activity. All rats maintained stable body weight and behavioral patterns, without any noticeable abnormal reactions or pain-related behaviors. After one month post-operation, the tails of rats in the sham operation group, IVDD group, and microsphere treatment group remained mobile and flexible, devoid of swelling or discernible differences. At the two-month mark post-surgery, the tails of the sham operation

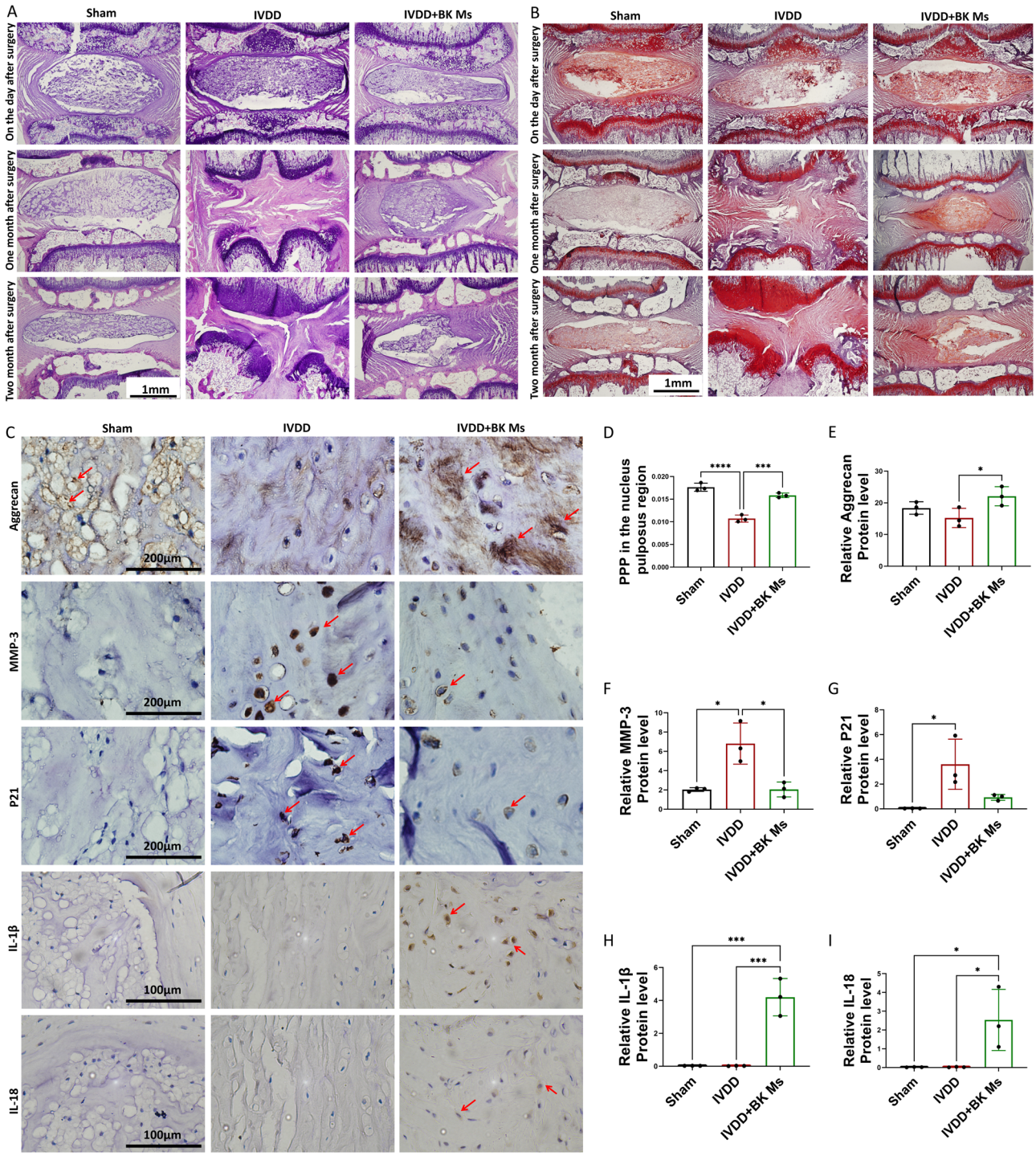

Fig. 8 | Histological and immunohistochemical analysis of intervertebral discs post-surgery. A HE staining of intervertebral disks 1 day, 1 month, and 2 months after surgery. **B** Safranin O-fast green staining of the intervertebral disc 1 day, 1 month, and 2 months after surgery. **C** IHC: Aggrecan, MMP-3, P21, IL-1β and IL-18 staining in intervertebral disks two months after surgery. Red arrows indicate positive cells. **D** PPP(Percentage of Positive Pixel) in the nucleus pulposus region. **E** Relative Aggrecan protein levels. **F** Relative MMP-3 protein levels. **G** Relative P21 protein levels. **H** Relative IL-1β protein levels. **I** Relative IL-18 protein levels. To assess the statistical differences between various groups, we employed one-way analysis of variance (ANOVA) followed by Tukey's post hoc test for multiple comparisons (*: $p < 0.05$, **: $p < 0.01$, ***: $p < 0.001$, ****: $p < 0.0001$). At each time point, each group consisted of three rats (n = 3).

group retained their flexibility without deformity. In contrast, the IVDD group exhibited partial enlargement of tails with slight deformities and reduced flexibility. Conversely, the microsphere treatment group displayed good tail mobility without deformities. Gross observations at the two-month post-surgery juncture revealed that the tail skin of rats in the normal group and IVDD model group displayed chloasma, indicative of notable age-related pathological changes in the model group. Conversely, the PLGA/BK microsphere treatment group exhibited fewer instances of chloasma on their tail skin, suggesting a certain degree of pathological relief in this treatment group (Fig. 7A).

X-ray observation using a molybdenum target

Concurrently, mammography X-rays of the tail were conducted (Fig. 7B, D–F) to further investigate the impact of IVDD and PLGA/BK microsphere

treatment on vertebral bone quality. This analysis focused on the upper and lower endplates of the intervertebral disks and the vertebral bodies, assessing their height changes and bone-related alterations. The results indicated that there were no significant changes in intervertebral height on the day after the operation. One month post-operation, an analysis of bony intervertebral height in the sham operation group, IVDD group, and microsphere treatment group demonstrated findings consistent with those obtained from MRI scans. Importantly, two months post-surgery, the IVDD group exhibited reduced intervertebral height along with minor vertebral bone hyperplasia. In contrast, the microsphere treatment group displayed smaller intervertebral height changes compared to the IVDD group, with no noticeable bony alterations.

MRI observation

Magnetic resonance imaging (MRI) scans were performed to assess the intervertebral disks of the tail vertebrae in each experimental group on the day following the operation, one month later, and two months later. The findings (Fig. 7C, G–I) indicated that there were no conspicuous signal abnormalities in the nucleus pulposus on the day after the operation. One month post-surgery, the sham operation group exhibited a T2-weighted high signal in the nucleus pulposus, indicative of good hydration status, with the intervertebral height remaining within the normal range. In contrast, the IVDD group displayed the disappearance of the water signal in the nucleus pulposus, accompanied by a significant reduction in intervertebral height. Notably, in the microsphere treatment group, the water signal was higher than that of the IVDD group but lower than that of the normal group.

Histopathological HE and safranin-O/fast green staining observations

We conducted a 1-month EDTA decalcification process on intervertebral disc specimens harvested from experimental animals, euthanized at various time points: one day after surgery, one month post-surgery, and two months post-surgery. Following complete decalcification, the specimens were coronally sectioned (Fig. 8A, B).

At the one-month mark, HE staining results revealed that the intervertebral disc nucleus pulposus and annulus fibrosus remained structurally intact in the sham operation group. Conversely, in the IVDD group, there was a significant reduction in nucleus pulposus tissue, disruption in the annulus fibrosus structure, and a noticeable decrease in intervertebral disc height. In the microsphere treatment group, some nucleus pulposus tissue was preserved, accompanied by hyperplasia of NPCs. After two months, the IVDD group exhibited complete disappearance of nucleus pulposus tissue, further reduction in intervertebral height, and instances of endplate destruction. In the microsphere treatment group, most of the nucleus pulposus structure had degraded, with only a small amount of nucleus pulposus tissue remaining. This remnant tissue displayed cell proliferation and extracellular matrix production. While the decrease in intervertebral height was less severe compared to the IVDD group, it still remained lower than that of the sham operation group. Safranin-O/Fast Green staining corroborated these findings, and due to its particular staining properties, it was also observed that the microsphere treatment group produced more proteoglycans than the IVDD group (Fig. 8D).

Immunohistochemical observations

Similarly, we performed immunohistochemical staining on pathological sections of rat caudal disc nucleus pulposus specimens obtained two months postoperatively (Fig. 8C, E–G). The molecular markers selected for this experiment included aggrecan, indicative of extracellular matrix synthesis metabolism, MMP-3, a marker of degradative metabolism, and P21, associated with aging. Over time, we observed a significant increase in the expression of MMP-3 and P21 in the IVDD group compared to the normal and microsphere treatment groups. This increase reflects an intensified degradation of the extracellular matrix and the emergence of aging signs. In contrast, the microsphere treatment group, compared with the IVDD group, showed increased expression of aggrecan and decreased expression of MMP-3 and P21, suggesting an enhancement in extracellular matrix synthesis metabolism and a delayed aging process. Given the close link between BK and inflammation, we also examined the expression of inflammatory cytokines IL-1β and IL-18 in the nucleus pulposus tissues (Fig. 8C, H, I). Their expression was upregulated in the microsphere treatment group, indicating that BK microspheres also influence to the induction of inflammation within the nucleus pulposus to some extent.

Discussion

Cellular aging and extracellular matrix metabolism are fundamental to the etiology and progression of intervertebral disc degeneration (IVDD)[19]. This study explores a novel treatment strategy centered on the controlled and sustained-release of BK, targeting the mitigation of IVDD. Our previous research has demonstrated BK's multifaceted biological activities, including its anti-oxidative stress, anti-apoptotic properties, and its ability to promote cellular vitality[20]. Additionally, we observed high expression levels of KNG and B2R in degenerated human tissue samples, as well as in human and rat cells, which we hypothesize could represent a cellular protective mechanism during aging or in response to damage. We propose that kallikrein expression diminishes with cell damage and aging, impairing the cleavage of KNG and subsequently reducing BK production, thereby weakening its protective role. Analysis of nucleus pulposus samples from normal and degenerated intervertebral disks revealed a significant decrease in kallikrein and BK expression in degenerated tissues, suggesting that BK plays a critical role in IVDD, warranting further investigation into its specific mechanisms.

Through bulk RNA-seq, we identified key signaling pathways associated with BK, notably those involved in extracellular matrix metabolism, and the PI3K pathway. Subsequent cellular experiments confirmed that BK alleviates TBHP-induced cellular aging and modulates the synthesis and degradation of the extracellular matrix.

However, BK, being a short-lived peptide, is rapidly degraded in the body[21]. Small doses may be insufficient to achieve therapeutic effects, while large systemic doses can cause adverse reactions, such as hypotension and organ edema[22]. To address this, we proposed the development of a sustained-release delivery system for BK. Building on previous research, we selected carboxyl-terminated PLGA as the carrier due to its enhanced encapsulation efficiency for peptides and protein drugs. We engineered PLGA/BK sustained-release microspheres, optimizing encapsulation efficiency and drug release kinetics. This strategy not only improves therapeutic outcomes but also minimizes the risk of systemic side effects and reduces the complications associated with frequent punctures, such as nucleus pulposus dehydration and further IVDD. This delivery system is designed to maintain therapeutic BK concentrations locally within the intervertebral disc, thereby optimizing the therapeutic efficacy.

Using laser particle size analysis technology, we quantitatively determined the size distribution of the microspheres, which exhibited a normal distribution. Notably, a reduction in PLGA concentration was associated with the formation of smaller microspheres, significantly impacting their size. For instance, 100 mg of PLGA typically produces microspheres approximately 100 μm in diameter, which is the ideal size for injection. Scanning electron microscopy (SEM) results showed that microspheres produced with 50 mg of PLGA were slightly larger than those produced with 100 mg of PLGA, contrary to the findings from dynamic light scattering (DLS). This discrepancy may be due to the lower PLGA concentration causing the microspheres' surfaces to become uneven, irregular, and porous. Consequently, the microspheres appeared smaller in particle size analysis but larger under electron microscopy. Considering these factors, as well as the importance of structural uniformity and diameter, we selected a 100 mg PLGA solution for our studies.

In the development of PLGA/BK sustained-release microspheres, the BK release curve is a critical factor in evaluating its potential for IVDD treatment. To assess the sustained and effective release of BK, we conducted in vitro drug release experiments in PBS solutions at pH values of 7.4 and 6.5, simulating physiological conditions within the body and the acidic environment of the nucleus pulposus[23]. We regularly monitored the

cumulative and daily average release of BK. Notably, in PBS at pH 6.5, the microspheres demonstrated excellent release kinetics both at the beginning and towards the end of the experiment. Since PLGA is linked by ester bonds that are prone to hydrolysis under acidic conditions, the rate of ester bond cleavage accelerates in environments with lower pH. As the ester bonds in the PLGA microspheres hydrolyze, the structure becomes looser and more porous, increasing permeability and facilitating the release of drug molecules through the microsphere walls, thereby accelerating the drug release rate[24]. This finding suggests that the acidic environment enhances BK release from the microspheres, improves its sustained-release adaptability within the nucleus pulposus, and potentially boosts BK's therapeutic effects. However, our microspheres reached 80% drug release after one month. Although this sustained-release is superior to traditional administration methods, a release duration exceeding two months would be more ideal given the treatment cycle for degenerative diseases and our therapeutic goals. In future experiments, we plan to develop injectable hydrogel-loaded microspheres to achieve longer-term drug release.

Subsequently, we established an IVDD model in the rat caudal vertebrae using a fine needle puncture technique and applied PLGA/BK microspheres to assess their therapeutic effects in vivo. Histological analysis after treatment indicated that BK within the microspheres could regulate extracellular matrix synthesis and degradation, promote cell regeneration, and alleviate age-related degeneration. However, the implantation of PLGA/BK microspheres significantly elevated inflammation levels, suggesting a more complex relationship between inflammation and IVDD than previously recognized. These findings imply that inflammation alone does not fully account for IVDD, highlighting the need for deeper exploration into the interactions and mechanisms linking inflammation and IVDD.

The role of BK in apoptosis has been a topic of ongoing debate. While some studies suggest that BK exacerbates apoptosis through specific pathways, others, including our own, have demonstrated that BK exerts a protective, anti-apoptotic effect, potentially mediated via the PI3K/AKT pathway. These discrepancies may arise from variations in experimental conditions, such as BK concentration, exposure duration, and cell type. For instance, certain studies have shown that BK promotes apoptosis in rat renal tubular cells by upregulating caspase-9 through enhanced oxidative stress[25]. Similarly, another study reported that BK increased oxidative stress, leading to caspase-3 upregulation and apoptosis in rat brain astrocytes[26]. Additionally, research has indicated that BK induces oxidative stress, affects mitochondrial metabolism, upregulates Bax and caspase-3, downregulates Bcl-2, and promotes apoptosis in human endothelial cells[27]. Conversely, other studies have shown that BK downregulates caspase-3 via the AKT pathway, inhibits superoxide complex formation, mitigates oxidative stress, and protects glomerular proximal tubular cells[28]. Furthermore, the inhibition of caspase-3, combined with anti-oxidative stress, anti-autophagy, and anti-apoptotic effects, has been found to protect cardiomyocytes[29]. Our previous findings, along with the current results, further underscore the protective role of BK, highlighting its potential to alleviate apoptosis-related disc degeneration.

Overall, these in vivo study results demonstrate that treatment with PLGA/BK microspheres has the potential to reduce disc injury, alleviate changes in vertebral bodies, enhance disc hydration, and slow the progression of IVDD. However, the microsphere treatment was not able to fully restore disc function, and the issue of reduced disc height persists. Consequently, future research will need to focus on optimizing drug dosage, treatment duration, and evaluating the long-term effects of this therapy.

Based on these findings, we propose a novel treatment method for IVDD. Specifically, by locally applying BK in the form of sustained-release microspheres or combining it with bioinjectable hydrogels, it is possible to maintain effective drug concentrations within the nucleus pulposus over an extended period. This approach could help alleviate cellular aging and promote the synthesis of the extracellular matrix. Future research will be directed towards optimizing this treatment strategy, exploring additional molecular mechanisms, and evaluating the potential of gene interventions or specific BK receptor agonizts to enhance IVDD treatment outcomes and improve patient quality of life. Additionally, we plan to conduct long-term safety and efficacy follow-up studies to verify the feasibility and sustained effects of this method. These advancements offer new hope to IVDD patients and are expected to significantly improve their quality of life and rehabilitation outcomes.

Methods

Human ethics approval and collection and processing of intervertebral disc nucleus pulposus samples

This study received ethical approval from the Institutional Research Ethics Committee of the Second Hospital of Lanzhou University (Ethics Number: 2023A-278). Informed consent was diligently obtained from patients, adhering to rigorous ethical standards. All ethical regulations relevant to human research participants were followed. Patient inclusion criteria were established by excluding individuals with medical histories involving infection, tuberculosis, or tumors. Normal and degenerated intervertebral disc nucleus pulposus samples were differentiated based on MRI findings and assessed using the Pfirrmann grading method[30]. Normal samples were sourced from patients with juvenile idiopathic scoliosis, while degenerated samples were collected from patients who underwent disc herniation or disc fusion surgery. After surgery, nucleus pulposus samples were promptly immersed in 4% formaldehyde solution for preservation to maintain structural and cellular integrity. Stringent protocols were followed throughout sample collection and processing, and all samples were anonymized to ensure patient privacy and confidentiality. The management of collected samples adhered to ethical norms, legal mandates, and regulatory requisites.

Rat ethics approval and extraction of rat NPCs

Nucleus pulposus tissue samples were extracted from 2-month-old male SD rats provided by the Lanzhou Institute of Zoology, with prior approval from the Institutional Research Ethics Committee of the Second Hospital of Lanzhou University (Ethics Number: D2022-218). Stringent procedures for anesthesia and euthanasia were implemented to safeguard animal welfare and rights, complying with the experimental animal protection regulations of the Ministry of Science and Technology of the People's Republic of China. The extraction method is as follows: After anesthesia, a male SD rat weighing ~100 g was euthanized with 1% sodium pentobarbital and subsequently immersed in 75% alcohol for 5 minutes. The tail was excised using scissors under sterile conditions, and the tail vertebra fur was removed on a clean workbench. The tail vertebrae intervertebral disks were retained, soaked in PBS, and the nucleus pulposus tissues were dissected using a surgical blade. The extracted tissues were placed in a 3 cm culture dish containing DMEM/F12 medium and collagenase-II. Cellular dispersion was achieved by repeated pipetting, followed by inoculation into a 25 cm^2 culture flask. The primary NPCs used in experiments were derived from the 3rd to 8th generations.

To investigate the impact of BK on NPCs, Bulk RNA-seq in BK-Intervened NPCs analysis was conducted. Initially, cultured NPCs were subjected to BK intervention. The procedure entailed dividing NPCs into two groups: a control group (untreated) and an experimental group treated with 10 μM BK. Total RNA was subsequently extracted from NPCs using an RNA extraction kit. High-throughput sequencing technology was employed to sequence the extracted total RNA samples, followed by bioinformatic analysis encompassing data quality control, alignment to the reference genome, gene expression level analysis, identification of differentially expressed genes, functional enrichment, and pathway analysis. This comprehensive process provided Bulk RNAseq data for normal NPCs and BK-intervened NPCs, facilitating comparative investigations into BK's role in NPCs, particularly in the regulation of cell aging and extracellular matrix metabolism.

RNA extraction and quality control

Total RNA was extracted from cultured NPCs using the TRIzol Reagent (AG RNAex Pro Reagent, China). RNA degradation and contamination

were assessed by electrophoresis on a 1% agarose gel. The quantity of RNA was measured using both the Qubit 4.0 Fluorometer (Thermo Fisher Scientific, Waltham, USA) and the Nanodrop One spectrophotometer (Thermo Fisher Scientific, MA, USA). RNA integrity was accurately determined using the Agilent 4200 TapeStation system (Agilent Technologies, Waldbron, Germany).

Library construction and quality control

Library construction was performed using the ALFA-SEQ RNA Library Prep Kit (Alfa Genetics, China). The key steps included: a) Purification of mRNA from total RNA using poly-T oligo-attached magnetic beads. b) Fragmentation of mRNA using the RT Buffer provided in the ALFA-SEQ RNA Library Prep Kit. c) First-strand cDNA synthesis using random hexamer primers and reverse transcriptase, followed by second-strand cDNA synthesis using DNA polymerase I and RNase H. d) Terminal repair and 3' terminal adenylation. e) Adapter ligation, fragment selection, and purification. f) PCR amplification using Hi-Fi PCR Mix and primers. g) Purification of PCR products with magnetic beads, followed by evaluation of library fragment size using the Qsep400 high-throughput nucleic acid protein analysis system (Hangzhou Houze Biotechnology Co., LTD., China). The concentration of the final library was measured using the Qubit 4.0 Fluorometer (Thermo Fisher Scientific, Waltham, USA).

High-throughput sequencing

The transcriptome sequencing was conducted on the Illumina NovaSeq 6000 platform, generating paired-end 150 bp (PE150) reads. This high-throughput sequencing technology was chosen for its ability to produce large volumes of data with high accuracy, essential for comprehensive transcriptome analysis.

Methods and analysis of bulk RNA-seq in BK-intervened NPCs

The raw RNA-seq data generated in this study have been deposited in the GEO database under the accession number GSE277600. To ensure the accuracy and reproducibility of the results, bioinformatics analysis was conducted using a standardized pipeline. The key steps in this process included (Fig. S1):

Quality control

Raw sequencing data were preprocessed using fastp (v0.23.2) to ensure high-quality reads for downstream analysis. The following steps were performed: 1) Adapter Removal: Reads containing adapter sequences were identified and removed to prevent interference with downstream analyses. 2) Removal of Reads with Ambiguous Bases: Reads containing a high proportion of ambiguous bases (N) were filtered out. Specifically, reads were discarded if the proportion of ambiguous bases exceeded 10%, ensuring only reads with clear base calls were retained. 3) Quality Filtering: Reads were discarded if more than 40% of their bases had a quality score (Q score) below 20. This step ensures that low-quality reads, which could introduce errors, were excluded from the dataset. 4) Sliding Window Quality Trimming: A sliding window approach was applied to trim the reads. A window size of 4 bp was used, and reads were trimmed if the average quality within the window dropped below 20. This step removes low-quality ends of the reads, improving the overall quality of the data.

After this preprocessing, the clean reads were further processed to remove rRNA sequences by aligning them to the NCBI rRNA database using Bowtie2 (v2.4.5), ensuring only non-rRNA sequences were retained for subsequent analyses.

Reference genome alignment

Clean reads were aligned to the reference genome (Rat Genome, version Rnor_6.0) using HISAT2 (v2.2.1), a fast and efficient software for aligning transcriptome sequencing reads to a reference genome. The reference genome and annotation files were obtained from the genome website.

The alignment process involved the following steps: 1) Read Alignment: Clean reads were aligned to the reference genome using HISAT2, which utilizes hierarchical indexing to efficiently handle spliced alignments. The resulting alignment information, including the mapping positions of reads, was stored in Sequence Alignment/Map (SAM) format. 3) Conversion and Processing: The SAM files were then converted to their binary equivalent, BAM files, which are more compact and suitable for further processing. These BAM files were sorted to order the alignments by their positions on the reference genome, and duplicate reads, which may arise from PCR amplification, were filtered out using Samtools. 4) Result Statistics: Final alignment statistics were generated to provide insights into the alignment quality, including the number of reads successfully aligned to the reference genome and the percentage of mapped reads. This step ensures the reliability of the subsequent analyses.

Quantification of gene expression

Gene expression levels were quantified using RSEM (version 1.3.3), and read counts for each gene were calculated.

The TPM (Transcripts Per Million) values were computed to make gene expression levels comparable between different genes and different experiments.

PCA, correlation coefficient heat maps, and expression heatmaps were generated to assess the relationships between all samples.

Differential expression analysis

Differential expression analysis was conducted using DESeq2 (v1.34.0). Genes with an FDR ≤ 0.05 and $|\log2(\text{fold change})| \geq 1$ were considered significantly differentially expressed.

Functional enrichment analysis

GO and KEGG enrichment analyses were performed on the differentially expressed genes using clusterProfiler (v4.2.2). GO terms and KEGG pathways with an FDR ≤ 0.05 were considered significantly enriched.In the KEGG pathway analysis, we highlighted pathways highly relevant to cell aging and extracellular matrix metabolism.

Experimental grouping and processing methods

In this study, distinct experimental groups were established according to specific research objectives and treatment regimens. Detailed information on each experimental group, including group name, treatment substances, and methodologies, is as follows: 1) Control Group: Untreated cells serving as a reference for comparison with other experimental groups. 2) TBHP Group: Cells exposed to a 150 μM TBHP solution for 12 h to induce nucleus pulposus cell aging and degeneration[31]. 3) BK Group: Cells subjected to 10 μM BK exposure. 4) PI3K Inhibitor Group: Cells pretreated with 20 μM LY294002 (PI3K inhibitor) for 30 min before BK and TBHP treatment[32]. 5) B2R Inhibitor Group: Cells pretreated with 20 μM HOE140 (B2R inhibitor) for 30 min prior to BK and TBHP treatment[33].

These experimental grouping and processing methods enable the examination of the effects of different treatment conditions on cells and facilitate an in-depth exploration of BK, TBHP, PI3K inhibitors, and B2R inhibitors in cellular senescence and associated signaling pathways.

Western blotting (WB)

WB, a widely utilized technique for assessing protein expression levels and interactions, was employed in this study. The following antibodies and protein detection reagents were utilized: P-P53 Antibody (1:1000, ABclonal, China), P21 Antibody (1:1000, ABclonal, China), P16 Antibody (1:1000, ABclonal, China), Aggrecan Antibody (1:1500, Affinity, China), Collagen II Antibody (1:1500, Affinity, China), MMP-9 Antibody (1:1500, Affinity, China), MMP-3 Antibody (1:1500, Affinity, China), Anti-Actin Antibody (1:1500, Abcam, England), and the PI3K/AKT Signaling Pathway Panel (1:1500, Abcam, England). The experimental protocol involved a series of steps. Initially, proteins were extracted from either cells or tissue samples using RIPA lysis buffer. Subsequently, the protein concentration was meticulously quantified utilizing a BCA kit. To standardize protein concentrations, protein loading buffer was added to the samples, followed by

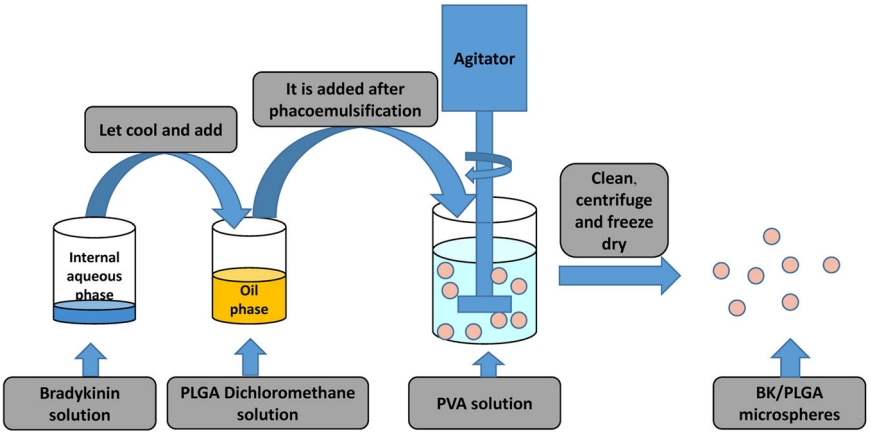

Fig. 9 | Schematic diagram of the preparation process of PLGA/BK microspheres.

denaturation through boiling. These denatured protein samples were then loaded onto an SDS-polyacrylamide gel for electrophoresis in Tris-glycine SDS buffer. This process separated the proteins based on their molecular weights, resulting in distinct bands representing different proteins. These separated proteins were transferred from the gel to a PVDF membrane. The PVDF membrane was then incubated with specific antibodies tailored to recognize and bind the target proteins. After primary antibody incubation, the corresponding antibodies were detected using HRP-labeled secondary antibodies, which were either goat anti-mouse or rabbit anti-mouse secondary antibodies. Finally, the relative intensities of the protein bands were quantified and analyzed using an imaging system. Through Western blotting technology, precise measurement of target protein expression levels across various experimental groups was achieved, enabling a comprehensive exploration of the functions and regulatory mechanisms of these proteins in processes related to cellular senescence, extracellular matrix dynamics, and associated signaling pathways.

Cell senescence β-galactosidase staining

Cell senescence was evaluated post-TBHP intervention using a cell senescence β-galactosidase staining kit. β-galactosidase is closely associated with cell senescence, with its expression level serving as a marker of senescence status[34]. This kit utilizes X-Gal as a substrate, producing a dark blue product under senescence-specific β-galactosidase catalysis. Visual assessment of β-galactosidase-stained cells, appearing blue under light microscopy, was performed. The experimental procedure involved fixing cells with a special staining fixative for 15 min, followed by PBS washing. Subsequently, cells were stained overnight at 37 °C with staining solution. Observation of cell senescence in each group was conducted under an ordinary microscope. β-galactosidase staining facilitated a straightforward and intuitive assessment of cell aging, providing a valuable experimental tool for further exploration of cellular aging mechanisms.

Immunofluorescence technology

Immunofluorescence experiments were employed to investigate the expression and localization of specific proteins. The antibodies used in the experiments included Aggrecan Ab (1:300, Affinity, China) and MMP-9 Ab (1:300, Affinity, China). In the immunofluorescence procedure, NPCs were cultured in a 6-well plate, and upon reaching 80% confluence, they were grouped and conditioned according to preset experimental criteria. Following intervention, cells were subjected to washing with PBS on a shaker, fixation with 4% paraformaldehyde, permeabilization with Triton X-100, blocking with 10% goat serum, and incubation with the corresponding primary antibodies overnight at 4 °C. Subsequent incubation with fluorescent secondary antibodies in the dark and staining of nuclei with DAPI working solution were performed. Fluorescence intensity of stained cells was measured using a fluorescence microscope at an excitation wavelength of 594 nm. Immunostained cells provided insights into the expression levels and subcellular localization of target proteins. Analysis of fluorescent signal intensity and distribution yielded quantitative data regarding protein location and relative abundance within cells, facilitating comprehension of cellular functions and molecular mechanisms.

Preparation and characteristic analysis of PLGA/BK sustained-release microspheres

In this section, we outline the methodical preparation and characterization of PLGA/BK sustained-release microspheres. Employing an orthogonal design methodology, we optimized the microsphere preparation process and conducted comprehensive analyses encompassing the methodology of PLGA/BK microsphere preparation, determination of drug loading and encapsulation rates, and drug release assessments under varying pH conditions. Furthermore, we performed cell co-culture experiments to assess the cytotoxicity of PLGA/BK microspheres.

Method for preparing PLGA/BK microspheres

The microspheres were synthesized using the double emulsion solvent evaporation technique (W/O/W), (Fig. 9)[35]. Initially, the internal aqueous phase was prepared by dissolving 1 mg of bradykinin (BK) in 0.5 ml of ultrapure water, ensuring both purity and precise dosing. Simultaneously, the oil phase was created by dissolving 200 mg of PLGA in 4.5 ml of methylene chloride using a vortex oscillator for a homogeneous solution. Ultrasonic emulsification followed, performed in three 10-second bursts with 3 s intervals, after incorporating the oil phase into the aqueous solution to produce a stable oil-in-water (O/W) emulsion with a milky white appearance. This emulsion was then slowly added dropwise to 40 ml of the external water phase containing 1% polyvinyl alcohol (PVA), continuously stirred overnight on a magnetic stirrer to facilitate the organic solvent's evaporation and form solid microspheres. A sample of the freshly prepared microsphere suspension was examined under a microscope at 40x, 100x, and 200x magnifications to assess the shape and size of the microspheres. After allowing the microspheres to stand for 1 h for precipitation, they were collected in a centrifuge tube, washed with ultrapure water, and centrifuged to remove unencapsulated drug and PVA solution, which is crucial for an accurate determination of drug load. The microspheres were then freeze-dried under vacuum, packed into 1.5 ml Eppendorf tubes, sealed in sterile paper-plastic bags, sterilized using cobalt-60 irradiation, and stored at 4 °C for future use, ensuring their stability and sterility for biomedical applications.

High-performance liquid chromatography(HPLC) analysis and BK standard curve generation

BK was precisely weighed and dissolved in PBS solution to create concentrations of 10 μg/ml, 20 μg/ml, 40 μg/ml, 80 μg/ml, 160 μg/ml, 320 μg/ml, 640 μg/ml, and 1280 μg/ml. The UV absorbance peak at 214 nm was measured using a HPLC analyzer[36], and a standard curve for BK in PBS solution

was constructed. The specific HPLC conditions included the use of a Kromasil C18 column (250 mm × 4.6 mm, 5 μm) maintained at 30 °C. The mobile phase consisted of a 0.01% trifluoroacetic acid (TFA) aqueous solution (A) and acetonitrile (B) system containing 0.01% TFA, with isocratic elution at a ratio of A:B (34:66 v/v) for 0 to 3 min. The flow rate was set at 0.3 mL/min, and an injection volume of 5 μL was used for detection at 214 nm.

Orthogonal design for microsphere preparation process optimization

We selected four factors with significant impacts on microsphere encapsulation and drug loading rates: A) oil phase (mass of PLGA added to dichloromethane, 4.5 ml); B) inner water phase (mass of BK in aqueous solution, 0.5 ml); C) outer aqueous phase (PVA solution concentration, 40 ml); and D) stirring speed. Employing encapsulation rate (S1) and drug loading rate (S2) as evaluation parameters, an orthogonal experimental design was employed to optimize the preparation process. The factor levels are presented in Table S1, and the orthogonal experimental design is detailed in Table S2.

Microsphere characterization

Following the optimization of the process, BK microspheres were collected via negative pressure freeze-drying. Visual observation was carried out, and a laser particle size analyzer was utilized to measure particle size, subsequently generating a microsphere diameter distribution chart. Additionally, a small quantity of each dry microsphere was subjected to gold sputtering, enabling the observation of microscopic shape, surface, and internal characteristics via scanning electron microscopy (SEM). Elemental composition analysis, encompassing carbon, oxygen and chlorine quantification, was also conducted to ascertain the microsphere's elemental composition.

Determination of drug loading rate, encapsulation rate, and drug release from BK-loaded microspheres

The drug loading rate was calculated as the drug mass in microspheres divided by the total mass of microspheres. The encapsulation rate was determined by dividing the total mass of drug in microspheres by the total mass of the input drug. To perform these calculations, 20 mg of dry BK sustained-release microspheres were weighed into a 1.8 ml test tube, and 300 μl of methylene chloride was added for thorough ultrasonic vibration. Following that, 1 ml of ultrapure water was introduced into the test tube, followed by mixing on a rapid mixer. After allowing it to stand for 10 minutes, the mixture was centrifuged at 12,000 rpm for 20 min. A 300 μl aliquot of the supernatant was taken, and its absorbance at 214 nm was measured using a HPLC analyzer. This process was repeated thrice to obtain an average value, which was used to calculate the quantity of encapsulated drug in the microspheres, utilizing the standard curve. The drug loading rate and encapsulation rate of the microspheres were then determined using the aforementioned formulas.

To assess drug release, three portions of 50 mg PLGA/BK sustained-release microspheres each were weighed and immersed in 10 ml of PBS (pH 7.4) and PBS (pH 6.5) solutions. These mixtures were sealed and placed in a 37 °C constant temperature shaker and agitated at a constant speed for 1, 2, 3, 7, 14, and 28 days. Following each duration, 0.5 ml of the solution was extracted for testing, with replacement by 0.5 ml of fresh PBS. After centrifugation, the supernatant was collected and subjected to high-performance liquid phase analysis to detect the absorbance peak at 214 nm. The standard curve was employed to calculate the released drug's concentration, enabling the determination of cumulative drug release and daily sustained-release rates.

In vitro biocompatibility of PLGA/BK microspheres

The in vitro biocompatibility of PLGA/BK Microspheres was evaluated by NPCs. Initially, rinse NPCs twice with PBS. Subsequently, 0.3 ml of trypsin was added for a 3 s digestion period. To terminate digestion, 4 ml of medium was added, and the culture bottle was rinsed repeatedly with a 1 ml pipette to suspend the cells evenly. NPCs were then inoculated into a 96-well culture plate at a concentration of 1 × 10^3 cells per well and incubated at 37 °C for 2 h to allow for cell adhesion to the plate. After adhesion, 1 mg PLGA/BK Microspheres suspended in complete culture medium were introduced to replace the original culture medium. Culturing with microspheres continued for 12 h, 1 day, 2 days, and 3 days. Culture medium waste was discarded at each time point, replaced with 100 μl of fresh complete culture medium, and 10 μl of CCK-8 reagent was added. Following 4 h of incubation at 37 °C, the optical density (OD) value at a 450 nm absorption wavelength was measured using a standard instrument for enzyme detection.

Establishment of rat IVDD model and animal experiment on local injection of PLGA/BK microspheres into the tail vertebra

In this section, we detail the establishment of a rat tail vertebra IVDD model via fine needle puncture of the intervertebral disc, as well as the subsequent local injection experiments involving PLGA/BK microspheres. Various assessment methods, including X-ray, MRI, pathology, and immunohistochemistry(IHC), were employed to evaluate the impact of PLGA/BK microspheres on IVDD, allowing for both quantitative and qualitative analyses of the degenerative progression.

Establishment and grouping of animal models

A total of twenty-seven Sprague-Dawley (SD) rats were randomly divided into three groups, with nine rats in each group. The sham operation group underwent a superficial procedure in which only a fine needle (outer diameter 0.5 mm) was used to puncture the skin after anesthesia. The model group and the treatment group, on the other hand, underwent intervertebral disc puncture to induce IVDD in the rat tail vertebrae[37]. Anesthesia was administered via intraperitoneal injection of sodium pentobarbital (40 mg/kg) based on the rats' body weight. Once anesthesia reached stability, the rats were positioned in a prone stance with their limbs secured. The tail of the rat was sterilized using 75% ethanol, and a sterile drape was utilized. A fine needle was employed to accurately puncture the caudal intervertebral disc, positioned 1 cm from the midpoint of the dorsal side of the caudal vertebra, until a sense of loss was perceived, indicating a depth of approximately 3 mm. The needle was rotated once to prevent penetration of the caudal vertebra and then slowly withdrawn. Sterile cotton swabs were used to apply pressure to the puncture site to control bleeding. In the treatment group, 2 μl of PLGA/BK microsphere suspension was injected into the original puncture site using a microinjector. In contrast, an equivalent volume of normal saline was injected into the IVDD group post-modeling. Following the procedure, the rats were returned to their cages, provided with sufficient food and water, and kept in a comfortable and quiet environment.

Postoperative management and observational parameters

Following surgery, the rats were individually housed in segregated cages based on their respective groups. Close monitoring of the surgical site in the tail vertebrae was conducted, focusing on parameters such as swelling, suppuration, infection, appetite, and mental state. The postoperative observational items are detailed in Table S3.

Magnetic resonance imaging (MRI)

To evaluate the progression of IVDD at specific postoperative time points, three rats from each group were randomly selected and humanely euthanized by cervical dislocation under anesthesia. The tail vertebrae were swiftly excised, and the intervertebral disks along with the adjacent upper and lower vertebrae of the target experimental segment were carefully removed and placed in 15 ml centrifuge tubes. These specimens were organized according to the experimental groups for subsequent examination of sagittal T2-weighted signal alterations in the rat intervertebral disc nucleus pulposus using MRI at the Magnetic Imaging Center of Lanzhou University Second Hospital.

The MRI scanning protocol employed a 3.0 T MRI scanner, with a 3.0 T 16-channel mouse coil positioned longitudinally. T2-weighted imaging (T2WI) was performed with the following specific parameters: repetition time (TR) = 2700 ms, echo time (TE) = 120 ms, matrix size of 256 × 256, scanning thickness of 2.0 mm, and an interval of 0 mm, encompassing a total of 11 levels. Following the scan, the outer fur of the tail vertebra was carefully removed, and the specimens were fixed in 15 ml centrifuge tubes containing 4% paraformaldehyde tissue fixative. This facilitated the observation of the hydration status of the nucleus pulposus within the tail vertebra intervertebral disks of the experimental rats.

Molybdenum target X-ray

Subsequent to this, at the designated postoperative time point, each group of experimental animals underwent molybdenum target X-ray inspection at the Imaging Center of Gansu Provincial People's Hospital. This provided foundation into alterations in bony gap height and vertebral bone quality within the tail vertebrae of the experimental rats.

Histopathology

Following the molybdenum target X-ray inspection, the paraformaldehyde-fixed caudal intervertebral disc specimens were subjected to immersion in EDTA decalcification solution and placed within a 37°C incubator. The decalcification solution was refreshed weekly until the caudal vertebra fine needle puncture site exhibited a soft tissue texture. Rat tail intervertebral disc samples were then fixed in paraformaldehyde solution for 24 hours, dehydrated through a series of ethanol concentrations, permeabilized with xylene, and embedded in paraffin. Subsequently, they were sectioned and subjected to histological staining, including Hematoxylin and Eosin (HE) and Safranin O-fast green staining. These standard staining methods allowed for the observation of intervertebral disc structure and composition. HE and Safranin O-Fast Green staining provided information on the morphology, composition, and pathological changes within intervertebral disc tissue, in accordance with kit instructions.

Immunohistochemical

Immunohistochemical analysis was conducted on human nucleus pulposus tissue and rat intervertebral disc tissue sections using immunoperoxidase technology. The sections were deparaffinized and subjected to heat-induced antigen retrieval using 0.1 M citrate buffer, followed by washing with phosphate-buffered saline (PBS). Peroxidase activity was quenched with 3% hydrogen peroxide. The slides were subsequently incubated with primary antibodies against BK (1:300), Kallikrein (1:300), Aggrecan (1:300), MMP-3 (1:300), and P21 (1:300). Immunohistochemical detection was performed in accordance with the instructions provided in the IHC kit. Finally, the sections were dehydrated using gradient concentrations of ethanol, sealed with neutral gum, and observed under a microscope.

Statistics and reproducibility

The data presented in this study were obtained from a minimum of three independent experiments, and all numerical results are expressed as the mean ± standard deviation (SD). Statistical analyses were conducted using GraphPad Prism software version 9, with one-way analysis of variance (ANOVA) followed by Tukey's post hoc test for multiple comparisons used to assess statistical differences between groups. A p-value less than 0.05 was considered statistically significant, with significance levels indicated as follows: $^{*}p < 0.05$, $^{**}p < 0.01$, $^{***}p < 0.001$, and $^{****}p < 0.0001$. Sample sizes for each experimental condition were set to 3, based on the prior experience of the research group and a review of relevant literature, or each experiment was repeated three times, with replicates defined as independent biological samples for both animal and cell experiments. For transcriptomic sequencing, technical replicates were performed to ensure consistency. For experiments without statistical analysis, reproducibility was assessed by conducting the experiments independently at least three times under the same conditions.

Reporting summary

Further information on research design is available in the Nature Portfolio Reporting Summary linked to this article.

Conclusion

In summary, our study highlights the significant impact of BK on IVDD and its promising therapeutic potential in managing degenerative disc conditions, with the PI3K pathway identified as a viable therapeutic target. Despite the inherent limitations of BK as a small molecule peptide, which restricts its broader clinical applicability, we successfully developed and optimized PLGA/BK sustained-release microspheres through an orthogonal design approach. These microspheres demonstrate uniform particle size, sustained drug release, and excellent biosafety profiles. Moreover, they effectively modulate the dysregulated extracellular matrix metabolism seen in IVDD, thereby slowing ECM imbalance progression and partially restoring nucleus pulposus function. This therapeutic paradigm shows substantial promise not only for IVDD treatment but also for broader applications, offering a valuable foundation for future research aimed at enhancing patient outcomes and quality of life in those affected by this condition.

Data availability

The raw transcriptomic sequencing data have been deposited in the GEO database (accession number: GSE277600). Uncropped and unedited blot/gel images are available as Fig. S5 in the Supplementary Information PDF. The raw data for quantitative analyses presented in the figures can be found in the Supplementary Data Excel file. All other data are available from the corresponding author upon reasonable request.

Received: 14 November 2023; Accepted: 1 November 2024;
Published online: 20 November 2024

References

1. Li, J.-Q., Kwong, W.-H., Chan, Y.-L. & Kawabata, M. J. L. Comparison of in vivo intradiscal pressure between sitting and standing in human lumbar spine: a systematic review and meta-analysis. *Life* **12**, 457 (2022).
2. Newell, N. et al. Biomechanics of the human intervertebral disc: a review of testing techniques and results. *J. Mech. Behav. Biomed. Mater*. **69**, 420–434 (2017).
3. Cornaz, F. et al. Intervertebral disc degeneration relates to biomechanical changes of spinal ligaments. *Spine J.* **21**, 1399–1407 (2021).
4. Nouri, A., Tetreault, L., Singh, A., Karadimas, S. K. & Fehlings, M. G. J. S. Degenerative cervical myelopathy: epidemiology, genetics, and pathogenesis. *Spine* **40**, E675-E693 (2015).
5. Ekşi, M. Ş. et al. At what speed does spinal degeneration gear up?: Aging paradigm in patients with low back pain. *Clin. Neurol. Neurosurg.* **215**, 107187 (2022).
6. Fenn, J., Olby, N. J. & science, C. S. C. I. C. J. F. i. v. Classification of intervertebral disc disease. *Front. Vet. Sci.* **7**, 579025 (2020).
7. Prado, M., Mascoli, C., & Giambini, H. Discectomy decreases facet joint distance and increases the instability of the spine: a finite element study. *Comput. Biol. Med.* **143**, 105278 (2022).
8. Zhou, J., Mi, J., Peng, Y., Han, H. & Liu, Z. Causal associations of obesity with the intervertebral degeneration, low back pain, and sciatica: a two-sample Mendelian randomization study. *Front. Endocrinol.* **12**, 740200 (2021).
9. Maher, C., Underwood, M. & Buchbinder, R. Non-specific low back pain. *Lancet* **389**, 736–747 (2017).
10. Fernandez, M. et al. Surgery or physical activity in the management of sciatica: a systematic review and meta-analysis. *Eur. Spine J.* **25**, 3495–3512 (2016).
11. Ohnishi, T., Iwasaki, N. & Sudo, H. J. C. Causes of and molecular targets for the treatment of intervertebral disc degeneration: a review. *Cells* **11**, 394 (2022).

12. Phan, K., Thayaparan, G. K. & Mobbs, R. J. J. B. Anterior lumbar interbody fusion versus transforaminal lumbar interbody fusion–systematic review and meta-analysis. *Br. J. Neurosurg.* **29**, 705–711 (2015).
13. Lad, S. P. et al. Complications, reoperation rates, and health-care cost following surgical treatment of lumbar spondylolisthesis. *J. Bone Joint Surg. Am.* **95**, e162 (2013).
14. Cheng, S. et al. Identification of aberrantly expressed genes during aging in rat nucleus pulposus cells. *Stem Cells Int.* **2019** 2785207 (2019).
15. Noda, M., Sasaki, K., Ifuku, M. & Wada, K. Multifunctional effects of bradykinin on glial cells in relation to potential anti-inflammatory effects. *Neurochem. Int.* **51**, 185–191 (2007).
16. Yu, J. et al. Kininogen 1 and insulin-like growth factor binding protein 6: candidate serum biomarkers of proliferative vitreoretinopathy. *Clin. Exp. Optom.* **97**, 72–79 (2014).
17. da Costa, P. L. N. et al. The kallikrein-Kinin system modulates the progression of colorectal liver metastases in a mouse model. *BMC Cancer* **18**, 1–9 (2018).
18. Zhu, X., Zheng, X., Wu, Y. J. B. & communications, b. r. Cleaved high molecular weight kininogen stimulates JNK/FOXO4/MnSOD pathway for induction of endothelial progenitor cell senescence. 450, 1261–1265 (2014).
19. Song, C. et al. Cellular senescence – Molecular mechanisms of intervertebral disc degeneration from an immune perspective. *Biomed. Pharmacother.* **162**, 114711 (2023).
20. Qiu, X. et al. Bradykinin protects nucleus pulposus cells from tert-butyl hydroperoxide-induced damage and delays intervertebral disc degeneration. *Int. Immunopharmacol.* **134**, 112161 (2024).
21. Hofman, Z., de Maat, S., Hack, C. E. & Maas, C. Bradykinin: inflammatory product of the coagulation system. *Clin. Rev. Allergy Immunol.* **51**, 152–161 (2016).
22. Ellison, N., Behar, M., MacVaugh, H., Marshall, H. & Marshall, B. E. Bradykinin, plasma protein fraction, and hypotension. *Ann. Thorac. Surg.* **29**, 15–19 (1980).
23. Liu, J. et al. Biological behavior of human nucleus pulposus mesenchymal stem cells in response to changes in the acidic environment during intervertebral disc degeneration. *Stem Cells Dev.* **26**, 901–911 (2017).
24. Tomic, I., Vidis-Millward, A., Mueller-Zsigmondy, M. & Cardot, J.-M. J. I. Setting accelerated dissolution test for PLGA microspheres containing peptide, investigation of critical parameters affecting drug release rate and mechanism. *Int. J. Pharm.* **505**, 42–51 (2016).
25. Chiang, W.-C., Chen, Y.-M., Lin, S.-L., Wu, K.-D. & Tsai, T.-J. Bradykinin enhances reactive oxygen species generation, mitochondrial injury, and cell death induced by ATP depletion—a role of the phospholipase CCa^{2+} pathway. *Free Radic. Biol. Med.* **43**, 702–710 (2007).
26. Yang, C.-M. et al. Multiple factors from bradykinin-challenged astrocytes contribute to the neuronal apoptosis: involvement of astroglial ROS, MMP-9, and HO-1/CO system. *Mol. Neurobiol.* **47**, 1020–1033 (2013).
27. Niewiarowska-Sendo, A., Kozik, A. & Guevara-Lora, I. Influence of bradykinin B2 receptor and dopamine D2 receptor on the oxidative stress, inflammatory response, and apoptotic process in human endothelial cells. *PLoS One* **13**, e0206443 (2018).
28. Hagiwara, M., Shen, B., Chao, L. & Chao, J. Kallikrein-modified mesenchymal stem cell implantation provides enhanced protection against acute ischemic kidney injury by inhibiting apoptosis and inflammation. *Hum. Gene Ther.* **19**, 807–819 (2008).
29. Wu, C. et al. Pretreatment of cardiac progenitor cells with bradykinin attenuates H2O2-induced cell apoptosis and improves cardiac function in rats by regulating autophagy. *Stem Cell Res. Ther.* **12**, 1–15 (2021).
30. Pfirrmann, C. W. J. R. Can MR imaging be used to predict the degree and prognosis of peripheral nerve injuries? *Radiology* **247**, 301–302 (2008).
31. Xie, L. et al. Circ ERCC2 ameliorated intervertebral disc degeneration by regulating mitophagy and apoptosis through miR-182-5p/SIRT1 axis. *Cell Death Dis.* **10**, 751 (2019).
32. Hou, G. et al. Down-regulation of Rictor enhances cell sensitivity to PI3K inhibitor LY294002 by blocking mTORC2-medicated phosphorylation of Akt/PRAS40 in esophageal squamous cell carcinoma. *Biomed. Pharmacother.* **106**, 1348–1356 (2018).
33. Wirth, K. et al. DesArg9-D-Arg[Hyp3,Thi5,D-Tic7,Oic8]bradykinin (desArg10-[Hoe140]) is a potent bradykinin B1 receptor antagonist. *Eur. J. Pharmacol.* **205**, 217–218, (1991).
34. Lin, J. et al. SIRT3 mitigates intervertebral disc degeneration by delaying oxidative stress-induced senescence of nucleus pulposus cells. *J. Cell Physiol.* **236**, 6441–6456 (2021).
35. Qiu, X. et al. Experimental study of β-TCP scaffold loaded with VAN/PLGA microspheres in the treatment of infectious bone defects. *Colloids Surf. B Biointerfaces* **213**, 112424 (2022).
36. Gao, C. et al. Development of a thiolysis HPLC method for the analysis of procyanidins in cranberry products. *J. Agric. Food Chem.* **66**, 2159–2167 (2018).
37. Zhu, D. et al. Periostin promotes nucleus pulposus cells apoptosis by activating the Wnt/β-catenin signaling pathway. *FASEB J.* **36**, e22369 (2022).

Acknowledgements

This work is supported by National Natural Science Foundation of China (82272536), Medical Innovation and Development Project of Lanzhou University (lzuyxcx-2022-190), Longyuan Youth Innovation and Entrepreneurship Talent Team Project (2024QNTD07), Natural Science Foundation of Gansu Province, China (24JRRA575). The Graphical Abstract was created with BioRender.com.

Author contributions

Xiaoming Qiu: Investigation, Formal analysis, Validation, Writing—original draft, Funding acquisition. Yizhi Zhang: Investigation, Validation, Writing—review & editing. Ziyan Wei: Methodology, Writing—review & editing. Zhangbin Luo: Conceptualization, validation. Zhuanping Wang: Writing—review & editing. Xuewen Kang: Validation, Resources, Funding acquisition.

Competing interests

The authors declare no competing interests.

Additional information

Supplementary information The online version contains supplementary material available at https://doi.org/10.1038/s42003-024-07196-0.

Correspondence and requests for materials should be addressed to Xuewen Kang.

Peer review information *Communications Biology* thanks Li Xiao, Auhin Maparu, Dong Wang, and Gaia Andreoletti for their contribution to the peer review of this work. Primary Handling Editor: David Favero. A peer review file is available.